Check for updates

2D/2D nitrogen-doped graphitic carbon nitride/cobalt sulfide nanostructures for fast photodegradation of methylene blue dye and real industrial sewage effluents†

Sai Bhargava Vuggili, [iD] [a] Umesh Kumar Gaur,[b] Tushar Tyagi[c] and Manu Sharma [iD] *[a]

Currently, the pollution of water and air is causing many diseases in humans and water pollution from textile industries is causing various problems for the livestock. To deal with this, photocatalytic degradation by g-C_3N_4-based nanocomposites has been trending in the scientific world. It is believed that doping with metals or nonmetals and constructing a nanocomposite with a metal sulfide can establish suitable energy band positions and a bandgap as an interface between two semiconductors, thus enhancing photodegradation efficiency. Herein, nitrogen-doped g-C_3N_4/CoS (CSNG) nanocomposites have been synthesized using a facile polycondensation-hydrothermal method by varying the concentration of nitrogen-doped g-C_3N_4 (NG). The CSNG-2 nanocomposite showed maximum photocatalytic efficiency (0.03474 min^{-1}) and adsorption capacity (~192 mg g^{-1}) as compared to NG and cobalt sulfide (CS). The results suggest that industrial real samples (RS), RS.I and RS.II, were degraded by 60% and 41% in 20 and 70 min, respectively. A mixture of RS.I with Methylene Blue (MB) dye solution, degraded 79% and 98% in 20 min, and RS.II with MB solution degraded 72% and 99% in 40 min. Scavenger and stability studies were performed with the CSNG-2 nanocomposite to determine the roles of organic species and photocatalytic efficiency during the photocatalytic mechanism. Superoxide played an important role in the photodegradation of MB and showed excellent photostability in five consecutive cycles with a loss of just 0.7%. Thus, our research highlights improved photocatalytic activity in the degradation of MB and industrial real samples with the enhanced photostability of CSNG nanocomposites, and the CSNG-2 nanocomposite can also be very useful in water-splitting and CO_2 reduction, *etc.*

Environmental significance

Today, the primary challenge of the human society involves reducing the burden of energy consumption and environmental degradation. Waste in the form of solids or liquids (organic pollutants) is increasing daily because of the manufacturing and building of new industries, which also disturbs the environment. Water contamination is being caused by a variety of businesses, including the textile, chemical, poultry, dairy, and pharmaceutical industries. Although many researchers have tried to treat these industrial wastewaters, we, the researchers from the Central University of Gujarat, Gandhinagar, India, are trying to make sure that these industrial wastewaters can be easily treated at a low cost to society. Herein, we report the effective degradation of organic pollutants, with good stability and great enhancement of our materials. This work provides a good platform for understanding the material properties and catalytic activity in the presence of visible light.

1. Introduction

Nowadays, there are two main challenges for human society, namely, to reduce the burden of energy consumption and

environmental pollution. Day-by-day the increase in the manufacturing and construction of industries causes increase the waste in the form of solids or liquids (organic pollutants), which also disturbs the environment. Various industries such as textile, chemical, poultry, dairy, and pharma, are discharging the wastes directly into the water, thus creating water pollution. These industries discharge toxic, carcinogenic, non-degradable wastes into the water bodies and cause severe problems for human life, aquatic life and also livestock. One of the major sources of water pollution is the presence of many pollutants in water, which are generated by textile industries through the use of different dye colorants.[1–7] In particular, textile industries

[a]School of Nano Sciences, Central University of Gujarat, Gandhinagar-382030, Gujarat, India. E-mail: manu.sharma@cug.ac.in
[b]VP & RPTP Science College, Vallabh Vidya Nagar, Anand-388120, Gujarat, India
[c]School of Engineering and Technology, National Forensic Sciences University, Gandhinagar-382007, Gujarat, India

† Electronic supplementary information (ESI) available. See DOI: https://doi.org/10.1039/d2va00208f

© 2023 The Author(s). Published by the Royal Society of Chemistry

Environ. Sci.: Adv., 2023, **2**, 795–814 | **795**

cause more severe damage to the environment because they use harmful chemicals such as organic pollutants, heavy metals, cationic dyes, anionic dyes, azo dyes, pesticides, and oils.[8–15] Among them, Methylene Blue (MB) is a common cationic dye that is toxic and carcinogenic and is especially used in food processing, pharmaceutics, printing, and textile industries. It has a molecular formula of $C_{16}H_{18}ClN_3S$, is odorless and is a dark green-colored powder but when added to water it appears as a blue solution at room temperature.[16] Different biological and chemical methods can be used for treating wastewater from different industries, namely, nano-filtration, advanced chemical oxidation, electro- and chemical coagulation, sedimentation, ultrasonic decomposition, and adsorption processes.[17] There are some disadvantages to these techniques such as high cost and excessive waste of energy, and the techniques are complicated.[18,19]

Among the various techniques, photocatalysis is one of the important and very useful techniques; it is cost-effective, easy, and stable with photocatalysts in the photocatalytic decolorization and degradation of organic pollutants.[20] Earlier, titanium oxide (TiO_2) was considered an excellent UV light-active semiconducting material for environmental remediation from wastewater and atmosphere pollution, H_2 production, and water splitting, due to its high stability, low cost, enhanced photocatalytic efficiency, and low-toxic nature.[7,21] Nevertheless, TiO_2 has major drawbacks that cause it to be unsuitable on an industrial scale; it possesses a wide bandgap of ~3.2 eV, which is applicable in UV radiation (conquering <5% of the solar spectrum) and fast recombination of photogenerated hole–electron pairs. Therefore, many attempts have been made to develop a semiconductor having a narrow bandgap in the visible region that can remove organic pollutants quickly and effectively.[21] Indeed, many photocatalysts have the properties of low quantum efficiency, high cost, high recombination rates, and less utilization of photogenerated charge carriers, which lead to low photodegradation efficiency.[7,21,22] Photocatalysts with Z-scheme heterojunctions can be used to explain the charge separation mechanisms. This is because of their exceptional light trapping and consumption abilities, spatially distributed reductive and oxidative active sites, and high redox capacities.[13,19]

Nowadays, two-dimensional (2D) materials have attracted much interest in fabricating novel photocatalysts and energy storage due to their excellent physicochemical, optical, electrical, and thermal properties.[23] 2D materials are also attractive because of their physical characteristics such as high elasticity, mobility, improved quantum transport, and electromechanical modulation.[24] Among the 2D materials, recently, the graphite-like two-dimensional structure with a metal-free polymeric semiconductor nature, named graphitic carbon nitride (g-C_3N_4), has been considered as an attractive nanomaterial in water splitting, remediation of organic pollutants, super-capacitors, sensing, drug delivery, and energy storage and hydrogen production.[25–27] It shows unique properties such as an excellent energy bandgap of 2.79 eV that can absorb visible light, high thermal stability (~600 °C), low-cost synthesis, excellent photochemical and physicochemical properties,

improved chemical properties (stable in organic, basic, and acidic solvents) and appropriate electronic band structure.[25–27]

It is well known that a material with a π-conjugated delocalized structure has a slow charge recombination rate of electron–hole pairs and fast charge separation efficiency. To date, numerous studies have been reported such as elemental doping with g-C_3N_4, morphology change, tuning of the bandgap, and heterojunction construction with g-C_3N_4 and semiconductors to improve the solar-light absorption to enhance photocatalytic efficiency.[28] However, g-C_3N_4 still has a few drawbacks such as low quantum efficiency, inadequate solar-light absorption, and high recombination rate of photoexcited electron–hole pairs. Due to these factors, it is believed that element doping can establish a suitable bandgap and band positions between the two materials, consequently enhancing the photodegradation efficiency. Among the elements, nitrogen (N) doping is easy and has shown improved catalytic properties with g-C_3N_4 nanostructures.[29–32] Vuggili *et al.* developed 2D/2D nitrogen-doped g-C_3N_4 with In_2S_3 nanocomposites for the photocatalytic degradation of dyes. The as-prepared materials resulted in ~99% photocatalytic degradation of MB dye in just 10 min with enhanced adsorption capacity. Industrial wastewater was also degraded by ~99% in 10 min with a cost-effective photocatalyst.[29] Xuli *et al.* synthesized nitrogen-doped carbon dots on g-C_3N_4/Ag_3PO_4 nanostructures for application in the photocatalytic degradation of organic pollutants. They showed that Methylene Blue (MB) and Rhodamine B (RhB) were degraded effectively in just 20 min and 15 min, respectively. The stability of the as-prepared photocatalyst was checked for four cycles with a slight loss of material. They concluded that nitrogen-doped photocatalysts played an important role in environmental remediation.[32]

Importantly, given the cost of photocatalysts, it is essential to replace noble metals with noble-free co-catalysts.[33] Noble-free-co-catalysts such as Cu, Ni, and Co-based sulfides or oxides show good adsorption and photocatalytic activity when combined with g-C_3N_4 nanostructures. Among them, cobalt sulfide (CS), a typical transition metal sulfide, is a good visible light active photocatalyst that has good chemical stability, reactivity, and high photocatalytic performance. CS nanostructures are also fabricated for different applications such as sensors, solar cells, water splitting, environmental remediation of pollutants in the air and water, electrocatalysis, and supercapacitors. Moreover, CoS nanostructures help to improve the lifetimes of photogenerated charge carriers and to boost the charge separation efficiency of the electron–hole pairs.[34–40] Recently, Khan *et al.* synthesized cobalt sulfide nanostructures as adsorbents and photocatalysts for the remediation of dyes. The as-prepared samples resulted in around 99% photodegradation and the maximum adsorption capacity of MB dye was found to be 629 mg g^{-1}. Stability was checked up to the 8th cycle with only negligible loss of the sample.[37] Wenqian *et al.* synthesized hollow cobalt sulfide nanospheres for the degradation of ciprofloxacin. They achieved 100% degradation of ciprofloxacin by CoS_2 hollow nanospheres at pH 8 in just 3 min with ~62% mineralization of ciprofloxacin.[41] Lylia *et al.* developed CoS-rGO by a solvothermal method for the degradation of

796 | *Environ. Sci.: Adv.*, 2023, **2**, 795–814

© 2023 The Author(s). Published by the Royal Society of Chemistry

RhB dye and pentachlorophenol in water. They found that the as-prepared material achieved the enhanced remediation of RhB and pentachlorophenol in just 10 min at room temperature. Indeed, the stability of the materials confirmed that the material was stable until the 8th cycle.[42]

Herein, we report a simple, efficient, and easy one-step hydrothermal method for the synthesis of g-C$_3$N$_4$/CoS nanocomposites by varying weight ratios of NG with CS for the degradation of methylene blue dye and industrial wastewater. This work highlights a simple and novel idea for the synthesis using self-heating and secondary calcination with metal sulfide for effective degradation.

2. Experimental section

2.1 Materials

The materials used included melamine (C$_3$H$_6$N$_6$, 99%, Sigma-India), cobalt nitrate hexahydrate (Co (NO$_3$)$_2$·6H$_2$O, 99% Sigma-India), trisodium citrate (Na$_3$C$_6$HO$_7$·2H$_2$O, 99% Sigma-India), triethanolamine (C$_6$H$_{15}$NO$_3$, SRL-India), ammonia solution (NH$_3$·H$_2$O, SRL-India), thiourea (CH$_4$N$_2$S, 99% Sigma-India), methylene blue (C$_{16}$H$_{18}$ClN$_3$S, 99.5% Sigma-India), and ethanol (C$_2$H$_5$OH, 99.5%). Throughout the experiment, Milli-Q water was used for preparing all the samples. All chemicals and Milli-Q water were used without any further purification. The quartz crucible and Borosil glassware, which were to be used in the experiment, were oven-dried before starting the experiment. Collected industrial samples were taken from Pirana Sewage Treatment Plant (180MLD) coordinated at 22° 58′ 51.2″ N latitude, 72° 32′ 36.8″ E longitude.

2.2 Synthesis of nitrogen-doped g-C$_3$N$_4$ (NG) nanosheets

Nitrogen-doped g-C$_3$N$_4$ (NG) nanosheets were synthesized according to our previous report.[29,31] A two-step process was used to synthesize NG. Firstly, 10 g of melamine was taken in a quartz crucible and kept for thermal polycondensation under an air atmosphere for 4 h at 500 °C. After cooling to room temperature, the solid particles were made into fine particles and kept for thermal polycondensation at 600 °C for 2 h under an air atmosphere for synthesizing nitrogen-doped g-C$_3$N$_4$ nanosheets. The product color was chrome yellow, and the final fine powder was used for further characterization. The sample was denoted as "NG".

2.3 Synthesis of the NG/CoS (CSNG) nanocomposites

We varied the amounts of NG with CS for fabricating NG/CS nanocomposites as 40 mg, 80 mg, and 160 mg. The said amounts were taken in different round bottom flasks containing 20 mL of Milli-Q water and sonicated for 20 min. After a homogeneous solution was obtained, 300 mg of Co (NO$_3$)$_2$·6H$_2$O was added to 20 mL of Milli-Q water, which turned into a pink solution, and stirred for 20 min at room temperature. Then, 150 mg of trisodium citrate (TSA), 2 mL of triethanolamine (TEA), and 8 mL of ammonia solution were slowly added with constant stirring while the color changed to a dark pink solution (A). Next, ~76 mg of thiourea was freshly prepared

in 10 mL of Milli-Q water (B), which was added to the solution (A) slowly with constant stirring for an hour. Finally, the solution was transferred to a 60 mL Teflon-lined-autoclave and placed in an oven for 6 h at 180 °C. After cooling, the solution was sonicated for 5 min and then washed 5 times with Milli-Q water and, subsequently, once with ethanol. Finally, the solutions were oven-dried overnight and denoted as "CSNG-1, CSNG-2, and CSNG-3", respectively. For comparison, cobalt sulfide was prepared under the same conditions, excluding NG, and denoted as "CS".[34]

2.4 Adsorption experiment

The adsorption capacities of the as-prepared samples were checked by adding 25 mL of MB dye solution (5 mg L^{-1}) to 25 mg of the photocatalyst, stirring for 20 min in dark, and analyzing with a UV-Vis spectrophotometer.

The adsorption capacities (q_e) of the as-prepared samples were evaluated using the following formula:[27]

$$q_e = \frac{(C_0 - C_e)}{M} \times V \tag{1}$$

where q_e (mg g^{-1}) is the adsorption capacity of the semiconducting material, C_0 and C_e (mg L^{-1}) are preliminary and outstanding absorbances of the solution at a time 't', the volume of the solution was V (L), and the mass of the sample was M (g).

2.5 Photodegradation of MB dye

The photocatalytic performances of NG, CS, and the CSNG nanocomposites were investigated using MB dye under visible light (tungsten lamp 200 W, $\lambda > 420$ nm). In brief, 25 mg of each photocatalyst was added to 25 mL of MB solution (10 mg L^{-1}) and stirred in the absence of light for an adsorption–desorption study for 20 min. The visible light source was turned on and the sample was collected, centrifuged and the supernatant was analyzed using a UV-Vis spectrophotometer.[25,27]

2.6 Free radical capture experiment

The detection of reaction species is similar to the photodegradation process. Various scavengers were used, including ethylenediaminetetraacetic acid (EDTA) as the hole (h$^+$) scavenger, 1,4-benzoquinone (BQ) as the superoxide ($^{\bullet}$O$_2^-$) scavenger, and isopropyl alcohol (IPA) as the hydroxyl scavenger. Each reaction solution consisted of 12.5 mL of 0.5 M scavenger, 12.5 mL of dye solution, and 25 mg of CSNG-2 nanocomposite.

2.7 Electrochemical testing

The Mott–Schottky analysis and electro-impedance spectroscopy (EIS) were performed on the Nova-Auto lab electrochemical analyzer by connecting potential and impedance modes. These tests were conducted by using a three-electrode set-up, with a saturated calomel electrode (SEC) as a counter electrode, a platinum wire as a reference electrode, and an FTO glass electrode as the working electrode. In the preparation of the working electrode, 4 mg of catalyst, 1 mL of IPA, 1 mg of carbon

black, and 10 μL of Nafion were mixed, sonicated, and stirred overnight to obtain a slurry that was coated on a 1 cm × 2 cm FTO glass, and was dried at 90 °C overnight in a vacuum.

3.   Results and discussion

3.1   X-ray diffraction (XRD)

Powder XRD is used for examining the phase, crystalline structure, and doping effects on the lattice structure of the as-prepared samples. XRD patterns of the N-doped g-C$_3$N$_4$ (NG), pristine CoS (CS), and CSNG nanocomposites are shown in Fig. 1. The XRD pattern corresponding to NG exhibited two diffraction peaks indexed as (100) and (002) at 2θ values of 13.03° and 27.7°, respectively. The XRD peaks were well matched to JCPDF no. 87-1526 with the monoclinic crystal phase of the material. However, a low-intensity peak at $2\theta =$ 13.03° indicated a crystal structure with an in-plane packing motif, signifying that pristine NG was a crystalline material. A high-intensity peak at $2\theta = 27.7°$ suggests the stacking plane of graphitic layers at an inter-planar distance of 0.325 nm.[31] The XRD peaks of pristine g-C$_3$N$_4$ suggested that the XRD pattern of NG caused no significant change in the diffraction peaks of pristine g-C$_3$N$_4$ but a very slight peak shift was observed at $2\theta =$ 27.04° with the same crystal structure of g-C$_3$N$_4$ nanosheets, Fig. S1.† The intensity of the characteristic peak ($2\theta = 27.7°$) showed a higher number of counts as compared to pristine g-C$_3$N$_4$, which is due to the doping with nitrogen and the crystalline nature of the sample. However, the peak at 27.7° signifies high-intensity counts as compared to pure g-C$_3$N$_4$, which may be due to the defects formed by nitrogen doping.[29]

From Fig. 1, we can see the diffraction peaks of CoS nanosheets (CS) indexed at (100), (101), (102), (110), and (202), which highlight 2θ values at 30.7°, 35.3°, 46.9°, 54.5°, and 74.9°, respectively, similar to JCPDS card no. 65-8977, Jaipurite CoS with a hexagonal structure and cell constants $a = 3.352$ Å, and $c = 5.138$ Å.[34] No CoO peaks or other diffraction peaks were detected in the sample, which indicated the pure Jaipurite

phase of the sample. The peak intensity of the composite indicated an increase in NG. The maximum intensity at $2\theta =$ 27.7° was observed for the CSNG-3 sample where the amount of NG was the maximum and the CSNG-1 sample showed no significant peak due to the minimal amount of NG.

3.2   Field emission scanning electron microscopy (FESEM)

FESEM analysis was done to observe the surface morphology as shown in Fig. 2. Fig. 2a shows the lamellar sheet-like morphology of NG. Fig. 2b shows the FESEM image of CoS with the wrapped sheet-like morphology and a thickness of ~50 nm.

Fig. 2c–e show the CSNG-1, CSNG-2, and CSNG-3 nanocomposites, where 2D/2D nanosheets of both materials were formed and showed good interaction with each other. This is due to the *in situ* hydrothermal synthesis of the CSNG nanocomposites, where the lamellar-like morphology was formed.[31] The elemental composition or percentage of CSNG-2 nanocomposite is shown in Fig. 2f. It confirms that all the elements such as C, N, Co, and S are present in the nanocomposite as displayed in the spectrum. The distribution of elements with contents of the CSNG-2 nanocomposite was determined by Energy Dispersive X-ray analysis (Fig. 2g–l). Elemental analysis of the CSNG-2 nanocomposite confirmed that C, N, Co, and S were present in the sample and indicated the homogenous distribution of elements in the CSNG-2 nanocomposite. Thus, elemental mapping results indicate that there were no impurities in the sample.

3.3   Transmission electron microscopy (TEM)

TEM, HRTEM, and SAED patterns of NG, CS, and the CSNG-2 nanocomposite were analyzed and are shown in Fig. 3. The TEM image of NG with the nanosheet-like morphology is shown in Fig. 3a. CS, which was prepared by a hydrothermal method with the effects of TEA, and NH$_3$ showed a flake-type morphology (Fig. 3b). The CSNG-2 nanocomposite looks like a nanosheet and exhibited layers of sheets or a wrapped sheet-type morphology that showed good interaction between NG and CoS (Fig. 3c). HRTEM images of NG, CS, and the CSNG-2 nanocomposite are presented in Fig. 3d–f. Lattice fringes were observed in the HRTEM image of CS, which corresponds to the interplanar distance of 0.65 nm with the (002) plane of CS nanosheets (Fig. 3e). No clear interplanar space was observed in NG and the CSNG-2 nanocomposite.

Diffraction spots obtained in the SAED image of NG (Fig. 3g) indicated the less-crystalline nature of NG. The CS nanosheets showed polycrystalline behavior with fewer spots (Fig. 3h). The SAED pattern of the CSNG-2 nanocomposite displayed a few concentric rings, which confirmed that the CSNG-2 nanocomposite was polycrystalline. From the TEM results, 2D/2D interactions of nanosheets were observed, and an interface was formed between the NG and CS. As a result, there was an enhancement in the splitting and transportation of photogenerated charge carriers and finally, an improvement in the photocatalytic activity of the photocatalyst.[31,34]
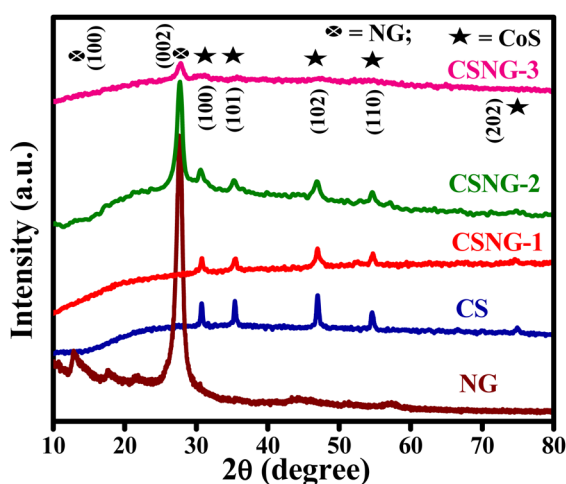

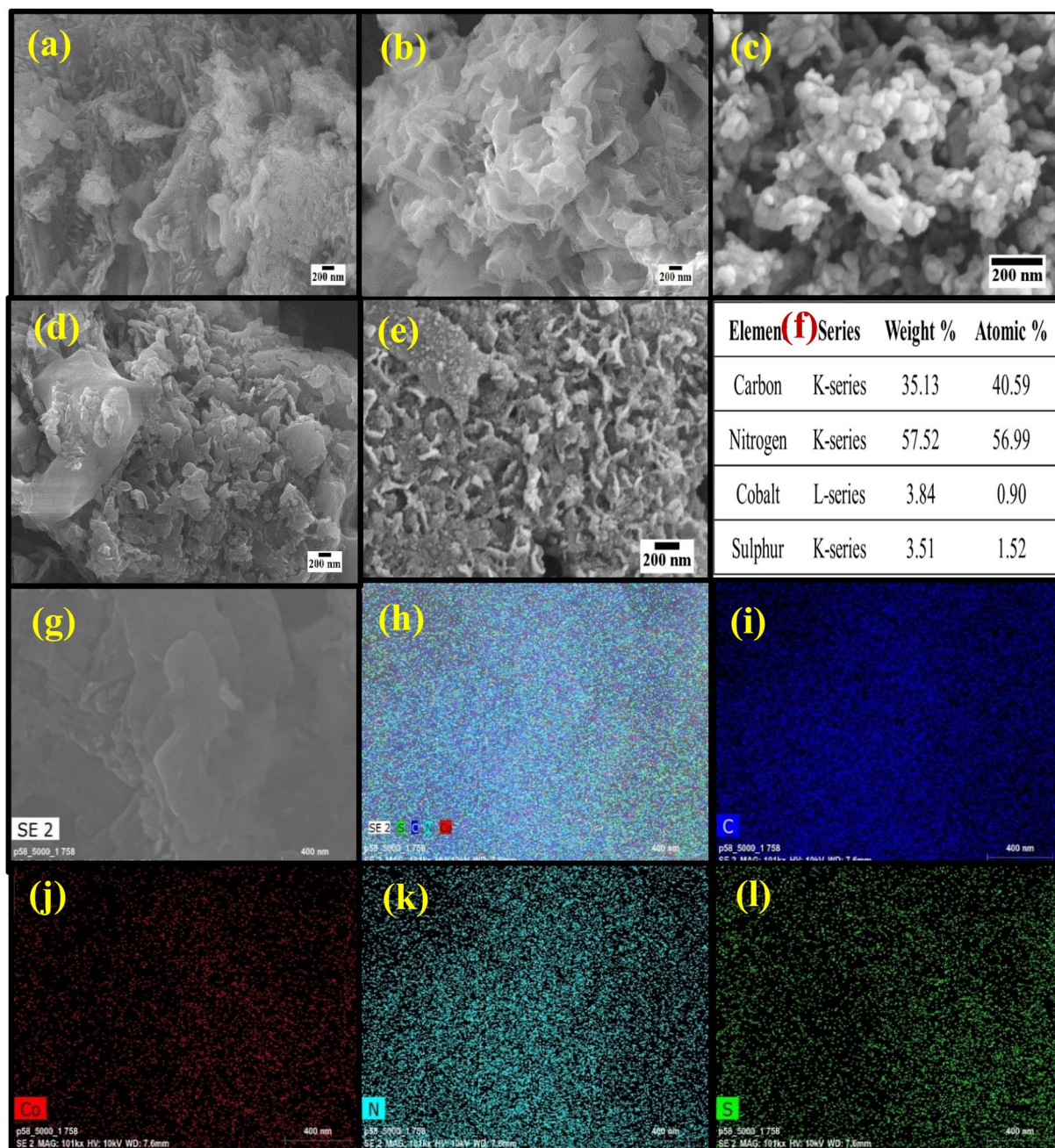Fig. 1   XRD of NG, CS, and CSNG nanocomposites.

Fig. 2 (a–e) FESEM images of NG, CS, and CSNG-1, CSNG-2, and CSNG-3 nanocomposites. (f) Elemental analysis of the CSNG-2 nanocomposite. (g–l) Elemental mapping of the CSNG-2 nanocomposite.

3.4 X-ray photoelectron spectroscopy (XPS)

The X-ray Photoelectron Spectroscopy (XPS) analysis was conducted to investigate the chemical valence states and surface chemical compositions of NG, CS, and the CSNG-2 nanocomposite. In the survey scan of NG, only three elements (C, N, and O) were observed. From Fig. 4c, carbon, and nitrogen may be attributed to g-C_3N_4, while oxygen may be due to the adsorption of oxygen-containing compounds (CO_2, O_2) on the surface of the compound. It is believed that the element nitrogen in graphitic carbon nitride has two main forms, *i.e.*,

the N–H bond, and melem units. As is known, when the nitrogen content increases, the N–H bonds decrease in the compound. Thus, the enhancement of the nitrogen content of melem units suggests that the doping of nitrogen was successful on the surface of the g-C_3N_4 nanostructure.

The deconvoluted contents of C 1s and N 1s chemical states are shown in Fig. 4a and b respectively. XPS spectra of C 1s were split into three main peaks at binding energies 284.6, 285.7, and 288.0 eV, which correspond to C–C, N=C–N, and C–NH$_x$, respectively. XPS spectra of N 1s showed three peaks at binding energies of 395.2, 396.8, and 401.1 eV with assigned chemical

© 2023 The Author(s). Published by the Royal Society of Chemistry

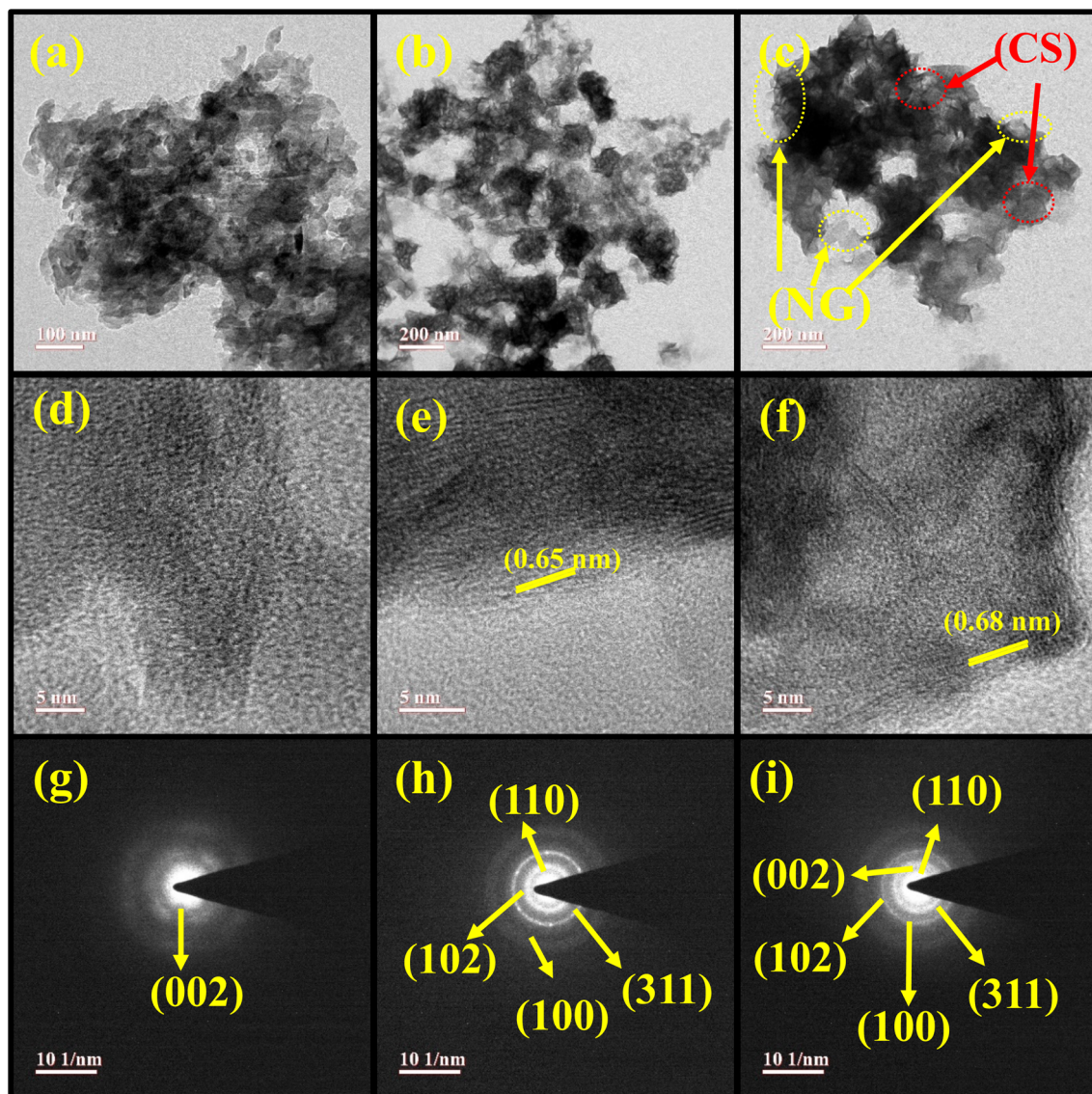*Environ. Sci.: Adv.*, 2023, **2**, 795–814 | **799**

Fig. 3 TEM images of (a) NG, (b) CS, and (c) CSNG-2. HRTEM images of (d) NG, (e) CS, (f) CSNG-2 with the corresponding SAED patterns of (g) NG, (h) CS, and (i) CSNG-2.

states of C=N–C, N-(C)$_3$, and C–N–H, respectively. The binding energy at 282.5 eV attributed to the sp^2 C–C bond, may be due to the adsorbed carbonaceous phase from amorphous carbon on the surface of g-C$_3$N$_4$. The binding energy at 285.8 eV for C 1s spectra is linked to sp^2-triazine rings in carbon bonds on the surface of g-C$_3$N$_4$.[31] A survey scan of NG confirmed that N, C, and O were present in the CS spectra (Fig. 4c). Moreover, valence states the elements comprising CoS were investigated by XPS measurements. A survey scan of CS confirmed that Co, S, C, and O were present in the CS spectra (Fig. 4f). From Fig. 4d, XPS spectra of Co 2p were investigated and peaks were observed at binding energies of 778.6 and 793.4 eV, which correspond to Co 2p$_{3/2}$ and Co 2p$_{1/2}$, while the binding energy at 795.6 eV showed a satellite peak in the Co 2p spectrum. XPS spectra of S 2p (Fig. 4e) were deconvoluted and resulted in two major peaks at binding energies of 161.8 and 162.9 eV, corresponding to S 2p$_{3/2}$

and S 2p$_{1/2}$, respectively, which suggests that the peak was due to the spin-orbital characteristic peaks of S$_2$$^{2-}$.[49,50]

According to the XPS analysis, NG and CS samples were successfully synthesized. XPS analysis of the CSNG-2 nanocomposite was also performed. Fig. 4k shows the full survey scan of the CSNG-2 nanocomposite in which C, N, Co, S, and O are visible. The presence of O in the spectrum may be due to the adsorbed content of oxygen molecules. The C 1s spectrum in Fig. 4g suggests three main peaks at binding energies of 284.9, 286.1, and 288.2 eV with the corresponding chemical bonds of C–C, N=C–H, and C–NH$_x$, respectively.

The peaks at 284.9 and 286.1 eV are linked to sp^2-hybridized bonds and may be due to the adsorbed carbon content on the surface of g-C$_3$N$_4$. The binding energy of N 1s (Fig. 4h) was divided into three peaks at 398.5, 399.2, and 400.7 eV, which were assigned to C=N–C, N–(C)$_3$, and C–N–H bonds,
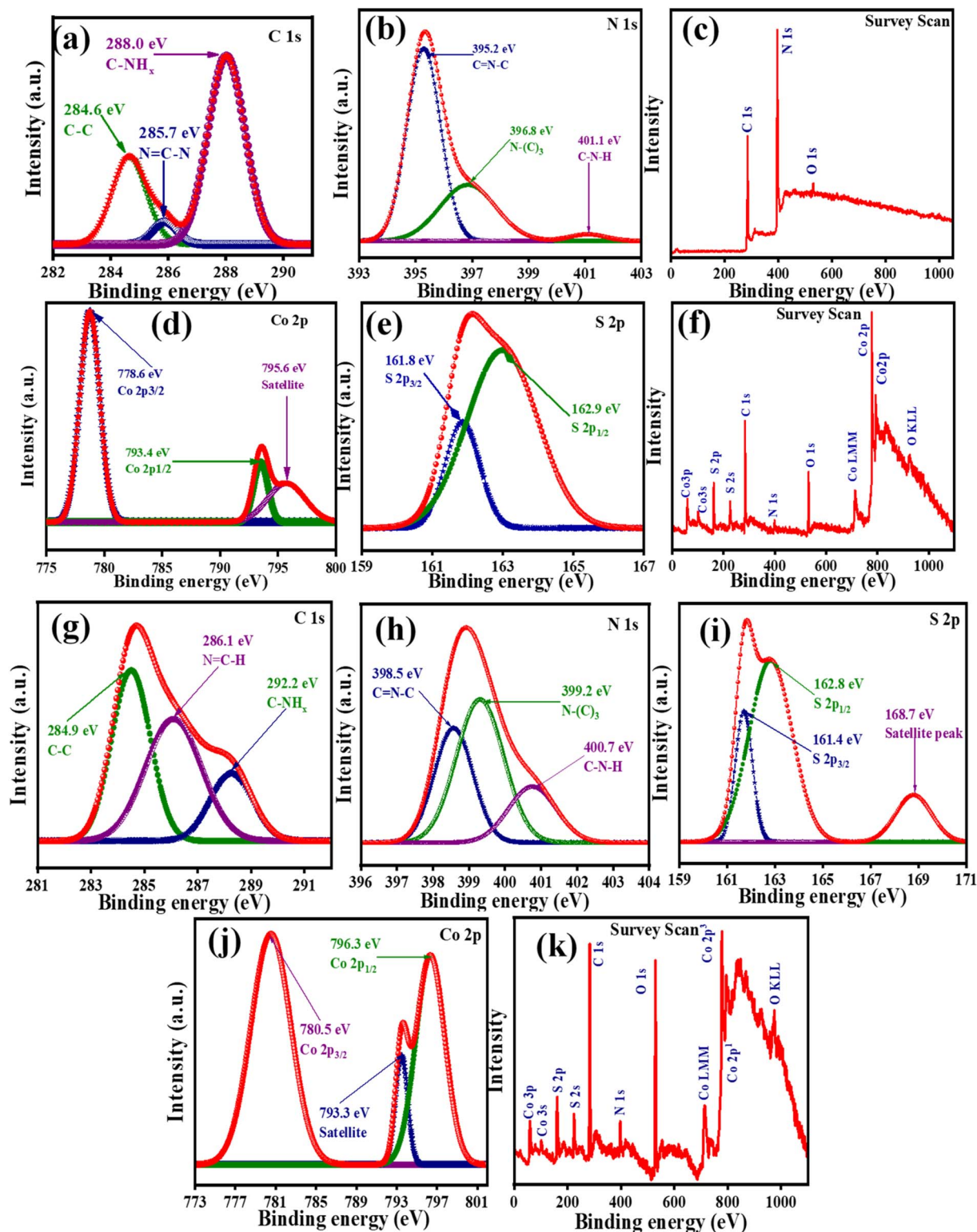
Fig. 4   High-resolution XPS peaks of (a–c) NG and (d–f) CS with the corresponding survey scan. (g–k) High-resolution XPS peaks with corresponding survey scan of the CSNG-2 nanocomposite.

respectively. The observed HR-XPS signals for S 2p (Fig. 4i) at 161.4 and 162.8 with corresponding satellite peaks at 168.7 eV were assigned to S $2p_{3/2}$ and S $2p_{1/2}$ respectively. These peaks suggest the presence of metal ions linked with S^{2-}.[42]

The XPS patterns of Co 2p (Fig. 4d) showed two obvious peaks at 780.5, and 796.3 eV corresponding to Co $2p_{3/2}$ and Co $2p_{1/2}$, respectively, with a satellite peak at 793.3 eV; these peaks indicate the presence of Co^{2+} ions on the surface of the CSNG-2

nanocomposite. The spectrum of the CSNG-2 nanocomposite shows that the peaks of C 1s, N 1s, and Co 2p shifted to higher binding energies in comparison to the pristine NG and CS nanosheets. These results indicate that the NG is well conjugated with the CS nanocomposite. Thus, binding energies with the physical environment of the as-prepared samples were changed due to the synergistic effect of NG and CS nanosheets and these results are well matched with the XRD and HRTEM results and suggest the successful formation of CSNG nanocomposites.

3.5 BET analysis

It is important to note that BET analysis is crucial by checking the surface area, pore size, and diameter of the materials during photocatalytic activity. A key stage in the remediation of organic pollutants is the adsorption process of organic pollutants in wastewater on the surface of the photocatalyst.

The driving forces for the adsorption isotherms that produce the N_2 in g-C_3N_4 can be provided by nitrogen doping with g-C_3N_4 nanosheets. Additionally, we may observe a wide range of size distribution because macropores and mesopores are present, and there are also little changes in pore width throughout all of the samples. As a result, all of the samples' pore size distributions fell within a small range of 10–20 nm while the pore volume was in the range of 0.95 cm^3 g^{-1} to 0.99 cm^3 g^{-1}, Fig. S2,† Table 1. From BET surface area analysis, it was observed and reported in our previous work that pure NG showed a surface area of ~29 m^2 g^{-1},[29] which may be due to the self-doping effect with nitrogen. The best as-prepared nanocomposite (CSNG-2) showed an active surface area of ~20 m^2 g^{-1}, Fig. S2.† The observed surface areas of both materials are very close and there was not much significant change in the surface area. Based on this observation, it can be concluded that the 2D/2D interaction of CS and NG was due to the synergistic effect of the material and suitable band positions, which make a perfect interface between the materials and reduces the charge recombination of the material and results in the photocatalytic activity of the materials. Moreover, the surface areas and pore volumes of the bare and best sample were too close and no significant changes were observed from the surface area measurement results, which indicated that the role of the surface area was not predominant in this system.

3.6 Raman spectroscopy analysis of NG and CS and the CSNG-2 nanocomposite

Raman spectroscopy is a nondestructive method for characterizing amorphous, crystalline, and nanocrystalline carbon. Fig. 5a shows that g-C_3N_4 particles were present on the surface,

i.e., peaks at 660–1750 cm^{-1}. The peaks at 726, 770, 986, 1220, and 1473 cm^{-1} are vibrations peaks assigned to the stretching and breathing bands of C–N aromatic heterocycles of melem. They also exhibited a D band and G band at 1329 cm^{-1} and 1548 cm^{-1}, respectively; this is due to the presence of graphite materials on the surface of the material. In the Raman spectrum of CS, peaks were observed at 346, 493, 529, and 686 cm^{-1}, which were assigned to the modes of T_{1g}, E_g, F_{2g}, and A_{1g} of CoS, respectively. There were slight shifts in peaks of NG (778, 923, 1345, 1486 cm^{-1}) and CS (329, 479, 680 cm^{-1}) in the Raman spectra of the CSNG-2 nanocomposite, Fig. 5c, which suggests that the heterojunction was formed by the NG and CS materials.[51–53]

3.7 Electrochemical impedance spectroscopy (EIS) analysis

Electrochemical impedance spectroscopy (EIS) was performed to study the kinetic electrode reactions and the charge separation and recombination process of NG, CS, and the CSNG-2 nanocomposite. It is well known that the improvement of charge carriers leads to enhancement in the electrical conductivity of semiconducting materials, and a smaller radius signifies less transfer resistance of the photogenerated charge carriers. The Nyquist plots of NG, CS, and the CSNG-2 nanocomposite are shown in the figure by plotting the Z' and $-Z''$ as real and imaginary impedances, respectively. These results suggest that NG and CS have bigger arc radii than the CSNG-2 nanocomposite in the Nyquist plot, which confirms that the CSNG-2 nanocomposite showed an improved charge separation rate of photogenerated charge carriers and effective electron transfer as compared to the bare NG and CS (Fig. 6).[13,19]

3.8 Reaction mechanism

For the synthesis of N-doped g-C_3N_4/CoS nanocomposites, melamine was heated to prepare bulk g-C_3N_4 by releasing the ammonia. Doping with a nitrogen atom narrows the bandgap and modifies the electronic structure of the semiconductor. In the formation process of CSNG nanocomposites, NG has a negative charge and Co has a positive charge on the surfaces. Therefore, NG and Co^{2+} were modified with sodium citrate, which formed a strong metal compound. TEA was used for hydrolysis by OH^- ions on the surface of the compound. With the help of ligands, Co^{2+} was gradually released and combined with OH^- ions to form a hydroxide template. The OH^- ions in the hydroxide template were substituted by S^{2-} and hydrolyzed when reacted with thiourea, forming the CSNG nanocomposite. Finally, depending upon the concentrations of the NG, cobalt, and sulphur precursors, the morphology, surface area, and electronic structure were changed in the semiconductor.[31,34,43,54–56]

3.9 Adsorption capacity and photocatalytic degradation of methylene blue

Adsorption studies were performed to check the ability of the as-prepared samples to adsorb Methylene Blue (MB) dye molecules under a veil of darkness. From Fig. 7a, it is seen that all the as-prepared samples (10 mg L^{-1}) adsorbed most of the MB dye

Table 1 BET analysis of NG and the CSNG-2 nanocomposite

Sample	S_{BET} (m^2 g^{-1})	Pore volume (cm^3 g^{-1})	Pore diameter (nm)
NG	28.54	0.956	18.19
CSNG-2	20.46	0.991	12.22

802 | *Environ. Sci.: Adv.*, 2023, **2**, 795–814

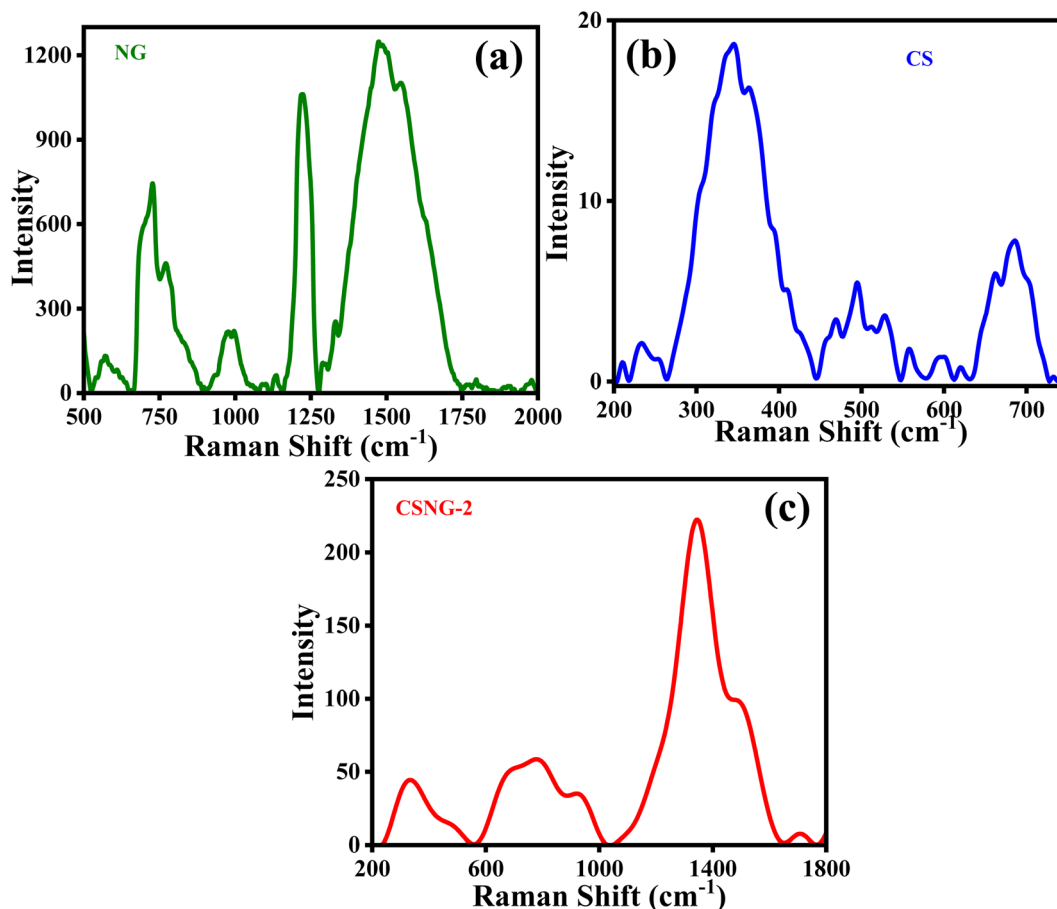© 2023 The Author(s). Published by the Royal Society of Chemistry

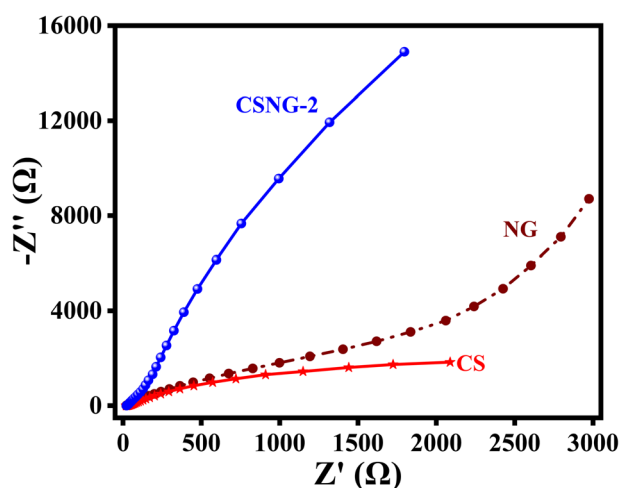Fig. 5 Raman spectra of (a) NG, (b) CS, and (c) CSNG-2 nanocomposite.

Fig. 6 EIS Nyquist plots of pure NG, CS, and the CSNG-2 nanocomposite.

molecules in just 10 min (~75% of total adsorption). As stated by Gupta *et al.*, a good adsorbent reaches the adsorption equilibrium point in a shorter period because of its large surface area and high porosity.[57] Moreover, it is believed that materials with a high surface area play a major role in the adsorption of

organic pollutants.[58,59] Fig. 7b displays the bar diagram of the equilibrium point of the adsorption coefficient of NG, CS, and CSNG nanocomposites in 40 minutes. As expected, CSNG-2 showed the maximum adsorption coefficient of 192 mg g^{-1}, which may be due to equal concentrations of compounds and synergistic effects between the compounds. NG and CS displayed adsorption capacities of 58 and 184 mg g^{-1}, respectively.

The adsorption percentages of the as-prepared photocatalysts are shown in Fig. 7c. The adsorption percentage of pure cobalt sulfide was found to be 81%, whereas, in pure NG, the adsorption percentage was only 26%, which is ~3.3-fold and ~1-fold those of bare CS and NG nanostructures. The improved adsorption percentage in the CSNG-2 nanocomposite sample may be due to the synergistic effect of both materials at an optimal weight ratio of CS and NG.

To examine the photocatalytic activity of NG, CS, and CSNG nanocomposites, MB dye was taken as a standard dye and the degradation process was conducted in the presence of visible light. At the outset, blank experiments with methylene blue dye were performed under the above-mentioned conditions. The standard MB dye concentration was 1.0×10^{-5} mol L^{-1}. There are two processes in the photocatalytic degradation of organic pollutants: adsorption (without light) and degradation of organic pollutants by the catalyst in the presence of visible

© 2023 The Author(s). Published by the Royal Society of Chemistry

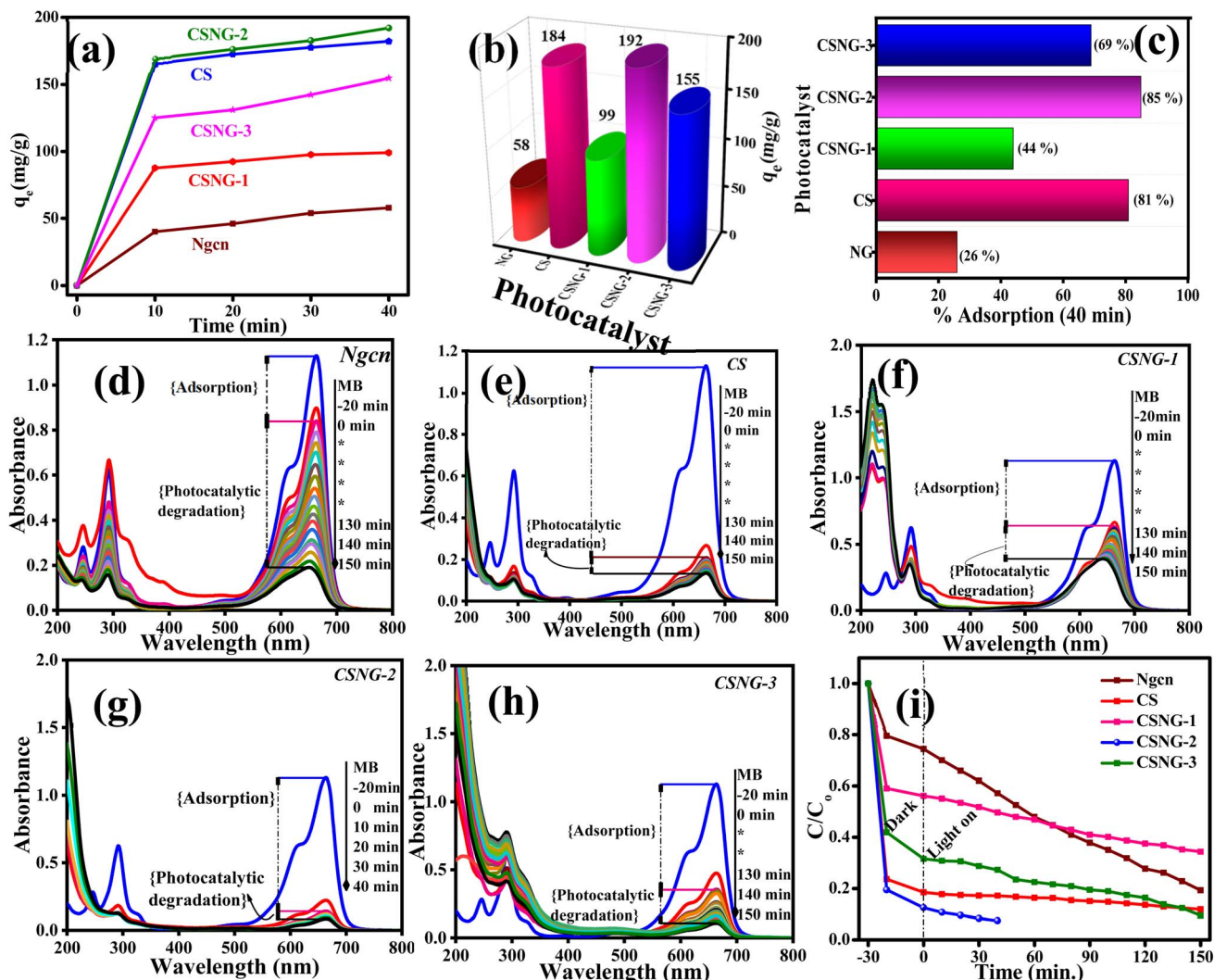*Environ. Sci.: Adv.*, 2023, **2**, 795–814 | **803**

Fig. 7   (a and b) Adsorption capacity study and (c) % adsorption of MB dye by NG, CS, and CSNG nanocomposites. Photocatalytic degradation of MB dye by (d–h) NG, CS, and CSNG nanocomposites. (i) Rate kinetics of NG, CS, and CSNG nanocomposites.

light.[25,27] In blank experiments, 25 mL of MB dye standard solution was taken, and it was degraded by only 10% in 150 min. Therefore, this states that MB dye did not degrade itself under visible light. Later, the same experiments were performed by as-prepared photocatalysts for the degradation of MB dye. The dye solutions were kept for adsorption studies in dark conditions. After the lamp was switched on and after every stimulated period of absorbance of the solution, the absorption was checked using a UV-Vis spectrophotometer for the degradation of MB dye at 663 nm wavelength. Here, we can see that in the presence of visible light and catalyst, the dye is rapidly degraded over time. From Fig. 7d–h, we can conclude that NG, CS, CSNG-1, and CSNG-3 were degraded by 83, 88, 90, and 72% in 150 min while CSNG-2 was degraded by 96% in just 40 min. This is due to interface formation between NG and CS nanosheets at an optimal concentration where the maximum degradation was achieved. The formation of a heterostructure and the synergistic effect of the nanocomposite resulted in enhanced photodegradation. g-C$_3$N$_4$ is a very good

photocatalyst while CS is a good adsorption material. Here, both materials play their roles in photocatalytic degradation. The total activity of the photocatalytic degradation of MB dye and industrial effluents depends on the interface and high surface area of the NG and CS. From Fig. 7i, we can see that the adsorption coefficient (stirring in the dark conditions) of NG is much lower compared to CS and other composites, and the photocatalytic activity of NG increases with the addition of the CS.

The rate kinetic studies showed first-order reactions by fitting the data of concentration versus time for the as-prepared photocatalysts. The observed rates of the reactions of NG, CS, CSNG-1, and CSNG-3 were obtained as 0.00836, 0.00593, 0.0087, and 0.00407 min^{-1}, respectively. The CSNG-2 nanocomposite showed the maximum rate constant of 0.03474 min^{-1}, which was ~4-fold and ~7-fold those of NG and CS, respectively, given in Table S1.† However, the enhancement in the reaction rate may be due to the synergistic effect of the NG and CS and the effect of equal concentrations of NG with CS, which is the

804 | Environ. Sci.: Adv., 2023, 2, 795–814

© 2023 The Author(s). Published by the Royal Society of Chemistry

Paper

optimal concentration where maximum photodegradation was achieved.

3.10 Adsorption kinetics

To explore the adsorption of the methylene blue dye mechanism by the as-prepared materials, a pseudo-first-order kinetic model was used to evaluate the adsorption result kinetics. The pseudo-first-order kinetic model is represented by the following equation:

$$\ln(q_e - q_t) = \ln q_e - k_1 t \qquad (2)$$

where k_1 (mg g^{-1}) is the first-order-rate constant, q_e (mg g^{-1}) is the adsorption capacity of methylene blue dye at the equilibrium stage and q_t (mg g^{-1}) is the adsorption capacity of methylene blue dye at time t. The values of q_e and k_1 were calculated from the linear graph $\ln(q_e - q_t)$ vs. t using the slope and intercept, respectively. The pseudo-first-order adsorption kinetics plot and table are shown in Fig. 8a and b, respectively.

Fig. 8a and b show the effects of the as-prepared nanostructures with the pseudo-first-order rate constants (Fig. 8b). The first-order-rate constant (k_1) values of NG, CS, CSNG-1, CSNG-2, and CSNG-3 are 0.0024, 0.0029, 0.0028, 0.0028, and 0.0027/min^{-1}, respectively. Moreover, the correlation coefficient (R^2) values were 0.966, 0.9194, 0.9165, 0.8854, and 0.8508 for NG, CS, CSNG-1, CSNG-2, and CSNG-3, respectively. The results suggest that a pseudo-first-order model controls the kinetic decomposition.

3.11 Photocatalytic degradation of industrial effluent (real sample, RS) analysis

To check the degradation performance of the real sample, the photodegradation of industrial wastewater was investigated by using the best catalyst (CSNG-2 nanocomposite) in the presence of visible light.[60] Herein, we have taken two sets of real samples and checked their photocatalytic activities. The two sets of samples are RS.I and RS.II, which are two different industrial

Table 2 Physicochemical properties of collected industrial samples

S. no.	Category	Result (RS.I)	Result (RS.II)
1	Colour	Pale yellow	Dark brown
2	pH	7.9	8.4
3	TDS (mg L^{-1})	1460	1850
4	TSS (mg L^{-1})	460	550

sewage discharges from the nearby industries of Pirana, Ahmedabad.[25,61]

The physicochemical parameters of the collected industrial samples (RS.I, and RS.II) are shown in Table 2.

Therefore, we prepared five series of samples for examining the photocatalytic activity of real wastewater samples.

(1) MB dye solution + catalyst

(2) RS.I + catalyst

(3) RS.I + MB dye solution + catalyst

(4) RS.II + catalyst

(5) RS.II + MB dye solution + catalyst

Fig. 9a–d shows UV-vis absorbance peaks at 270 nm, 275 nm, and 663 nm for RS.I, RS.II and MB dye, respectively. The UV absorbance peaks at 270 and 275 nm are due to pesticides such as clothianidin and thiamethoxam, or can be mixtures of organic compounds present in the wastewater.[62] The same process was performed for the photocatalytic degradation of real samples and a mixture of real samples and MB dye solution. Finally, we observed that RS.I and RS.II were degraded by ~67% and ~31% in 20 and 70 min, respectively.

Moreover, a mixture of RS.I with MB dye solution degraded 79% and 98% and RS.II with MB dye solution resulted in 72% and 99% degradation in 20 and 40 min, respectively. In the presence of the CSNG-2 nanocomposite, the mixture of real samples with MB dye sample was degraded effectively due to the collaborative interaction of NG and CS nanosheets. The photodegradation efficiency of organic pollutants was calculated by using the following formula:[27]

$$\eta = \frac{C}{C_o} \times 100 \qquad (3)$$

(b)

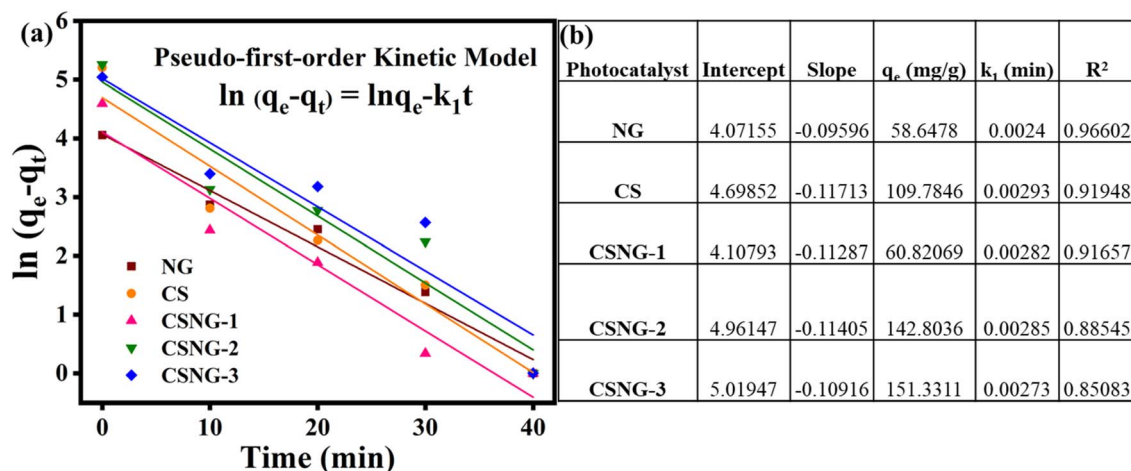| Photocatalyst	Intercept	Slope	q_e (mg/g)	k_1 (min)	R^2
NG	4.07155	-0.09596	58.6478	0.0024	0.96602
CS	4.69852	-0.11713	109.7846	0.00293	0.91948
CSNG-1	4.10793	-0.11287	60.82069	0.00282	0.91657
CSNG-2	4.96147	-0.11405	142.8036	0.00285	0.88545
CSNG-3	5.01947	-0.10916	151.3311	0.00273	0.85083

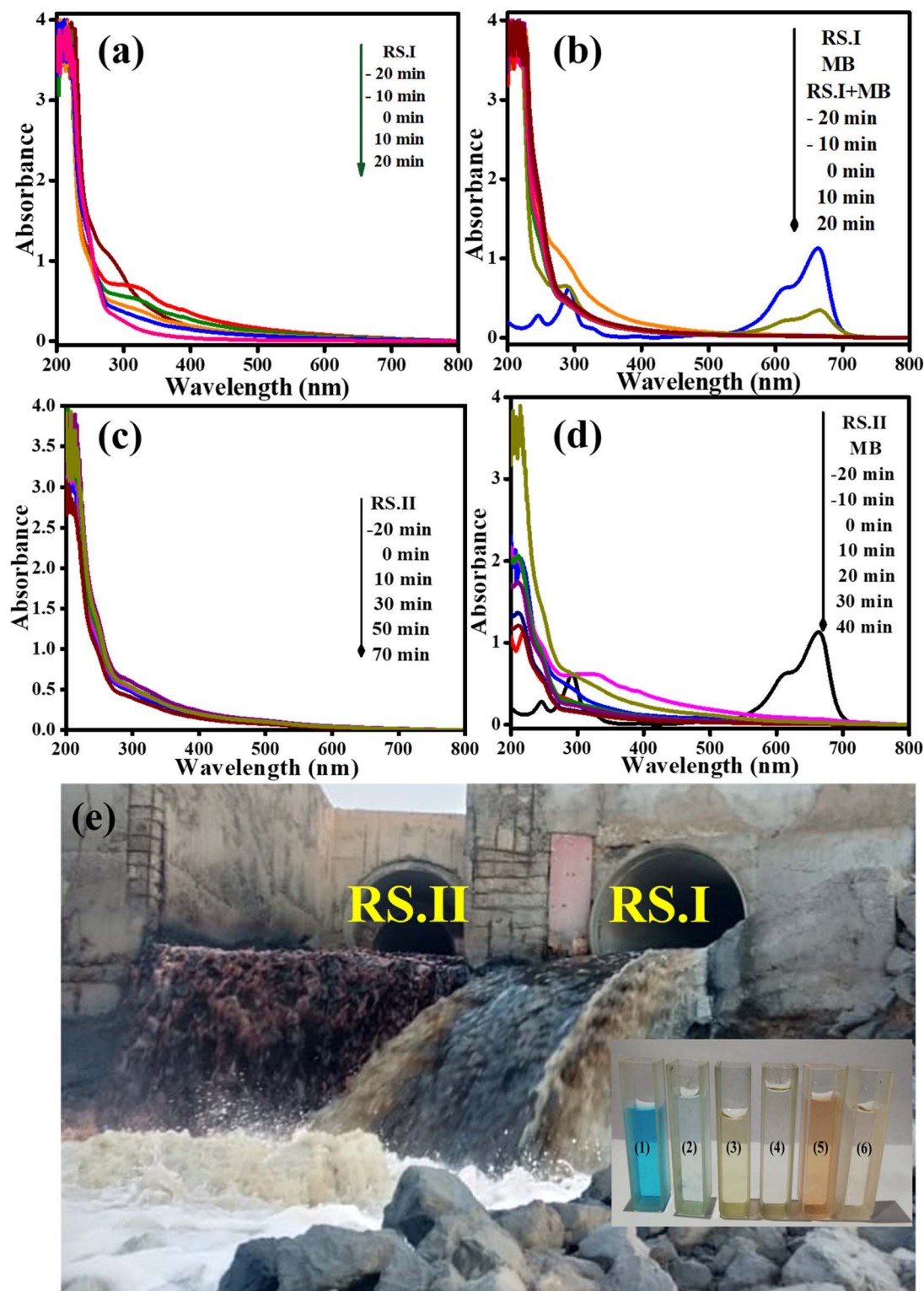**Fig. 8** (a and b) The pseudo-first-order-kinetic model with time.

Fig. 9 (a and c) Real sample analysis using the CSNG-2 nanocomposite with RS.I and RS.II, and (b and d) real sample analysis with MB dye using the CSNG-2 nanocomposite. (e) Real sample location sites (RS.I, and RS.II); the inset shows the digital images of MB, RS.I and RS.II before and after degradation with the catalyst, respectively.

where η is the efficiency, C_o is the concentration of pollutants at the initial stage, and C represents the concentration of pollutants at time t. Fig. 9e shows an image of the real sample collection site.

3.12 Scavenger and recyclability study

The photodegradation of organic pollutants generally takes place in the presence of radical formation. In catalytic reactions,

806 | Environ. Sci.: Adv., 2023, **2**, 795–814

© 2023 The Author(s). Published by the Royal Society of Chemistry

Fig. 10 (a) Scavenger study and (b) recyclability study on the CSNG–2 nanocomposite.

free radicals are the main reactive species to degrade the organic molecules. For a better understanding of the photocatalytic reactions, different types of scavengers were used to check the presence of reactive oxygen species (ROS). Isopropyl alcohol was used as a hydroxyl radical (HO$^\cdot$) scavenger, ethylenediaminetetraacetic acid (EDTA) acted as a hole (h$^+$) scavenger, while 1,4-benzoquinone (BQ) acted as a superoxide ($^\cdot$O$_2^-$) scavenger. The photodegradation efficiency of MB dye by the CSNG-2 nanocomposite was investigated under visible light with a control experiment (without scavenger) and with different types of scavengers (Fig. 10a). After the addition of scavengers to the CSNG-2 with MB dye solution, the BQ scavenger showed significant degradation (28%), suggesting that $^\cdot$O$_2^-$ played a major role as an active radical in photocatalytic degradation. EDTA and IPA scavengers degraded around 43% and 66%, indicating that h$^+$ and HO$^\cdot$ also played auxiliary roles in the degradation process.[27]

The recyclability study is said to be the most important feature for practical use in checking the stability of the catalyst. Five consecutive cycles of the photodegradation process under visible light were performed by the CSNG-2 nanocomposite, Fig. 10b, after which, the CSNG-2 nanocomposite showed a very

small reduction (~1%) in the degradation process, which may have decreased during washing after every cycle. This result confirmed that the stability of the CSNG-2 nanocomposite is quite good. Thus, the CSNG-2 nanocomposite possesses excellent stability, and can also be used to treat sewage wastewater.[27]

The morphological tests by FESEM before and after five consecutive recyclability reactions of MB dye by CSNG-2 nanocomposite were performed and are shown in Fig. 11a–b. This figure shows that there was not much change in morphology after the five consecutive photocatalytic reactions, thus confirming that the CSNG-2 nanocomposite has good morphological stability even after five consecutive photocatalytic reactions.[27]

3.13 Real sample analysis by GC-MS

We performed the analysis using GC-MS spectra for pure MB, and RS.II was collected near the Pirana Sewage Treatment Plant (180MLD) at 22° 58′ 51.2″ N latitude, and 72° 32′ 36.8″ E longitude. To check the role of the catalyst, we used the catalyst with MB dye, with RS.II and with a mixture of RS.II and MB dye solution after 40 minutes, as shown in Fig. S3.1 and S3.2.† At this point, the peak intensity was decreased because of intermediates or the opening of the ring structure of MB dye after the photocatalytic degradation of MB dye. These are the main possible organic species/intermediates that were degraded under the influence of light and in the presence of a catalyst for 20 minutes.

3.14 UV-vis, bandgap, Mott–Schottky, and band position analyses

UV-Vis absorption peaks of NG and CS are shown in Fig. S4.1.† The bandgap plays a prominent role in the photocatalytic degradation of organic pollutants. Thus, bandgaps of the as-prepared photocatalysts can be evaluated by using the following formula:[44,45]
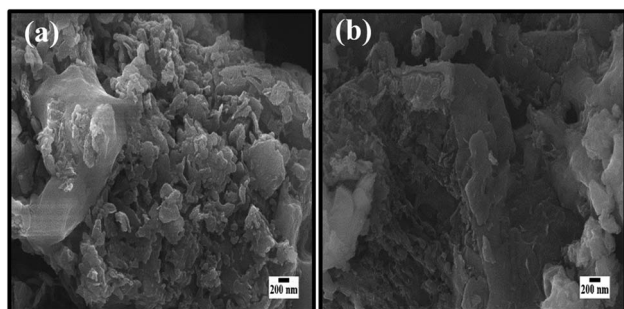

Fig. 11 The morphological information before (a) and after (b) recyclability tests after five consecutive recyclability reactions.
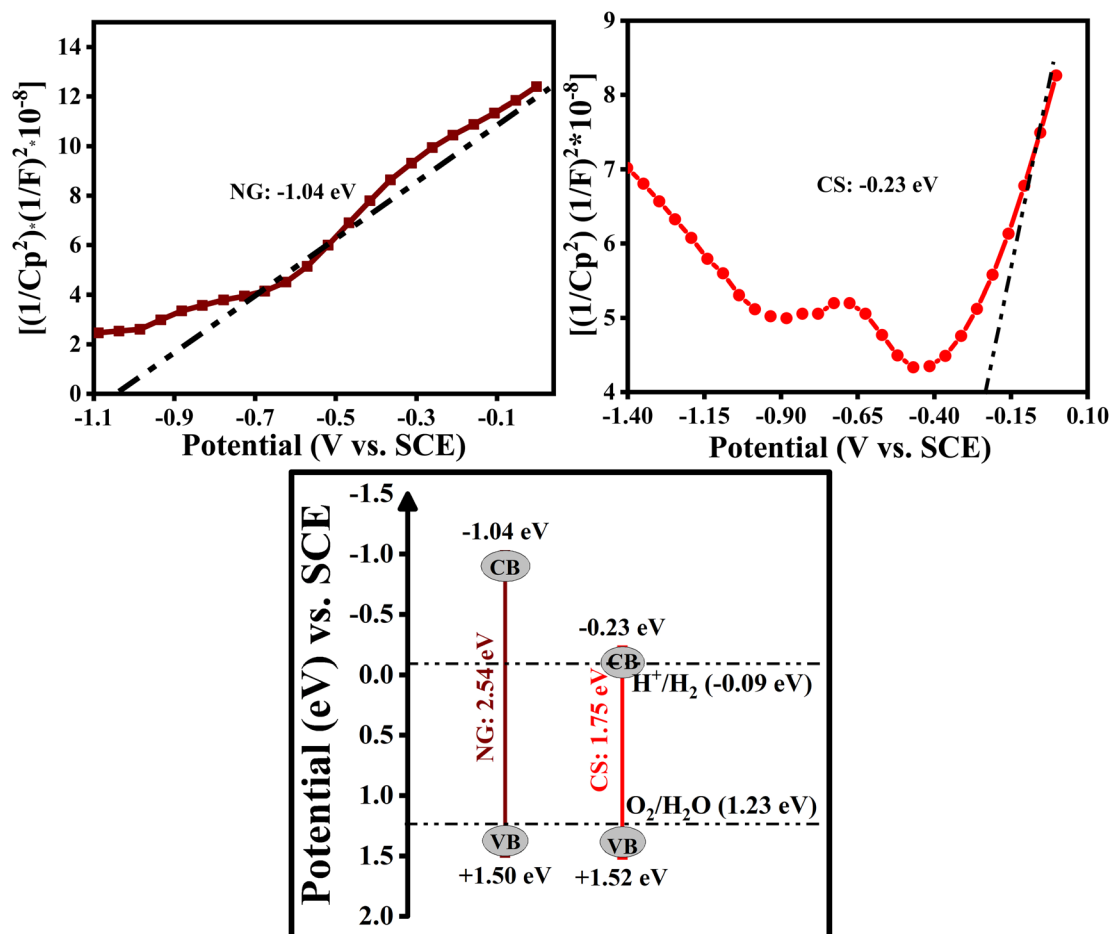
© 2023 The Author(s). Published by the Royal Society of Chemistry

Environ. Sci.: Adv., 2023, **2**, 795–814 | **807**

Fig. 12 Mott–Schottky analysis and band positions of NG and CS.

$$(\alpha h v)^n = A(h v - E_g) \qquad (4)$$

Here, α, h, v, A, E_g, n are the absorption coefficient, Planck's constant, frequency of light, proportionality constant, bandgap

energy, and integer, respectively. Importantly, from the above equation, 'n' plays a major part in confirming the bandgap energy of the material.
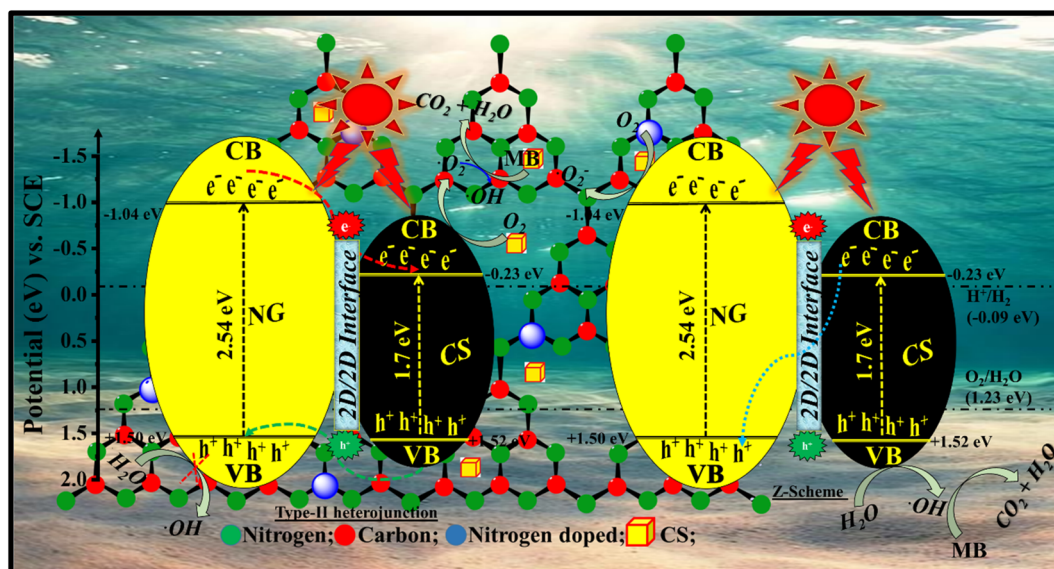

Fig. 13 The schematic representation of a photocatalytic mechanism.

© 2023 The Author(s). Published by the Royal Society of Chemistry

In the bandgap measurement, the bandgaps of bare samples (NG, CS) were calculated by using the Tauc plot method. NG showed an indirect bandgap, so for the calculation of the indirect bandgap, the following equation was used:

$$(a h v)^{\frac{1}{2}} = A(h v - E_g) \tag{5}$$

In the case of bare CS, the direct bandgap was calculated by using the following equation:

$$(a h v)^2 = A(h v - E_g) \tag{6}$$

In the case of nanocomposites, the bandgap measurement is difficult by using the Tauc plot method. This is because two different materials were present in the composites, which have different types of bandgap; *i.e.*, direct and indirect bandgaps.

Accordingly, the bandgap energy level of the as-prepared photocatalysts is an indirect bandgap because the achieved value of '*n*' in the above equation equals $\frac{1}{2}$ and 2. Therefore, the bandgap, *E* (eV), was obtained by the tangent to the horizontal axis of the planes which shows the bandgap of the semiconductors and was plotted (Tauc plot) against $(\alpha h v)^{\frac{1}{2}}$ *vs. E* (eV) as shown in Fig. S4.2.† The bandgaps of the as-prepared bare photocatalysts were calculated as NG: 2.54 eV, CS: 1.75 eV

Mott–Schottky plots were studied to further explain the photocatalytic mechanism and analyze the conduction band positions of NG and CS, which were measured at a frequency of 1 kHz, and are shown in Fig. 12. The NG and CS make a positive slope in the Mott–Schottky graphs, which indicates that NG and CS possess n-type semiconductor behavior. The calculated conduction band potentials of NG and CS were determined to be −1.04 eV and −0.23 eV *vs.* SCE. Therefore, by using the formula below, we can find the valence band positions of the as-prepared samples.[27,47,48]

$$E_g = E_{VB} - E_{CB} \tag{7}$$

where E_g is the band gap of the material, E_{VB} is the valence band position and E_{CB} is the conduction band position of the semiconductor.

By incorporating the as-obtained values in the above equation, the valence band positions of NG and CS are +1.50 eV, and +1.52 eV, respectively. By this, we can say that the photogenerated electron carriers are beneficial for charge separation between the NG and CS, which results in enhanced photocatalytic activity. As a result, the composite's CB potential electrons can combine with O_2 to make $^{\bullet}O_2^-$ but it is challenging for the composite's holes to oxidize OH^-/H_2O to produce the hydroxyl radicals $^{\bullet}OH$ in the photocatalytic process. This is congruent with the findings of an experiment using scavenger traps, which showed that the principal active species, $^{\bullet}O_2^-$, are immediately generated during the degradation process.[27]
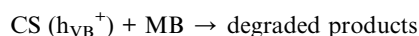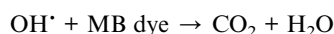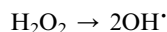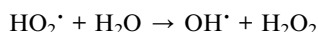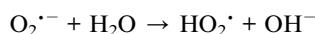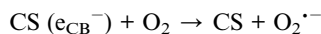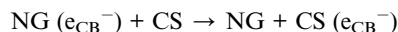
4. Photocatalytic mechanism

When visible light irradiates the surface of the photocatalyst, it produces photogenerated charge carriers that go from the valence band (VB) to the conduction band (CB). The photogenerated electrons get activated in the CB of NG and are transferred to the CB of CS and produce oxygen radicals. During this process, the rate of e^- transportation increases very quickly, and the charge is accommodated on material I to material II. This type of mechanism can be observed in type II semiconducting materials where the band positions of both materials are suitable for high charge transfer. These free electrons react with the surface O_2 molecules and produce superoxides that are finally converted into $^{\bullet}OH$ radicals. Holes in the VB of CS and NG react with water molecules to form $^{\bullet}OH$. Thus, these $^{\bullet}OH$ radicals behave like strong oxidizing agents and when

Table 3 g-C_3N_4-based nanocomposites for the degradation of organic pollutants from wastewater

Photocatalyst	Contaminants	Source of light	Reaction time, % degradation, or rate	Ref.
N–g-C_3N_4@In_2S_3 nanocomposites	Methylene blue	200 W tungsten bulb	10 min, 98%	29
N–ZnO-g-C_3N_4	Rhodamine B	500 W xenon lamp	180 min, 97%	63
O-doped g-C_3N_4	Bisphenol A	1000 W xenon lamp	180 min, 93%	64
Mpg-C_3N_4/Ag/ZnO nanowires	Direct orange 26	250 W mercury lamp	120 min, 94%	65
Thiophene-doped-g-C_3N_4	Bisphenol A	300 W xenon lamp	100 min, ~99%	66
O-doped g-C_3N_4	Rhodamine B	300 W xenon lamp	3 min, ~99%	67
Ag-g-C_3N_4/$LaFeO_3$	Methylene blue	300 W xenon lamp	90 min, ~98%	68
	Tetracycline		120 min, ~94%	
Multi-element doped g-C_3N_4	Naproxen	500 W xenon lamp	90 min, ~93%	69
Sm_2O_3/S–g-C_3N_4	Methylene blue	500 W xenon lamp	150 min, ~93%	70
Mn/P co-doped g-C_3N_4	Rhodamine B	500 W xenon lamp	150 min, ~99%	71
N-CQDs/g-C_3N_4/PDS	Tetracycline hydrochloride	500 W xenon lamp	60 min, ~90%	72
N-doped g-C_3N_4 nanotubes	Rhodamine B	350 W xenon lamp	60 min, ~94%	73
P-doped g-C_3N_4	Atrazine	500 W xenon lamp	30 min, 98%	74
Co–O–g-C_3N_4	Bisphenol A	500 W xenon lamp	100 min, 99%	75
C–g-C_3N_4/Ag_2O/α-Fe_2O_3	Acid red 14	SMD lamps	90 min, ~90%	76
KF, KCl, KBr doped g-C_3N_4	Methylene blue	250 W xenon lamp	100 min, ~99% (KF)	77
Ag–g-C_3N_4	Rhodamine B	300 W xenon lamp	30 min, ~93%	78
Boron-doped-g-C_3N_4	Rhodamine B	300 W xenon lamp	40 min, 100%	79
Ag-doped-g-C_3N_4	Methyl orange	300 W xenon lamp	10 min, ~87%	80

these radicals react with organic pollutants, that leads to photocatalytic degradation. A plausible photocatalytic mechanism for the degradation of MB dye molecules by the CSNG-2 nanocomposite is shown in Fig. 13, and the mechanism in equations is shown below.[25,46]

$$NG/CS + h\nu \rightarrow NG\ (e_{CB}^-) + CS\ (h_{VB}^+)$$

$$NG\ (e_{CB}^-) + CS \rightarrow NG + CS\ (e_{CB}^-)$$

$$CS\ (e_{CB}^-) + O_2 \rightarrow CS + O_2^{\cdot -}$$

$$O_2^{\cdot -} + H_2O \rightarrow HO_2^{\cdot} + OH^-$$

$$HO_2^{\cdot} + H_2O \rightarrow OH^{\cdot} + H_2O_2$$

$$H_2O_2 \rightarrow 2OH^{\cdot}$$

$$OH^{\cdot} + MB\ dye \rightarrow CO_2 + H_2O$$

$$CS\ (h_{VB}^+) + MB \rightarrow degraded\ products$$

Various materials with g-C$_3$N$_4$ were explored for developing effective nanostructures for the environmental remediation of organic pollutants from wastewater as shown in Table 3.

5. Conclusion

By a simple hydrothermal process, CSNG nanocomposites were successfully synthesized. All the photocatalysts were analyzed by XRD, UV-DRS, FESEM, EDX mapping, TEM, GC, and XPS techniques. In the first report on NG/CoS nanostructures for the photocatalytic degradation of MB dye and real samples, we have achieved enhanced adsorption capacity (192 mg g^{-1}) and photocatalytic degradation (96% in 40 min) by a CSNG-2 nanocomposite under visible light illumination. The CSNG-2 nanocomposite showed the maximum rate constant (0.03474 min^{-1}) that was ~4-fold, and ~ 7-fold those of NG, and CS, respectively. In addition, the CSNG-2 nanocomposite showed an adsorption capacity at 192 mg g^{-1}, which was ~3.3 fold, and ~1 fold those of bare NG and CS nanostructures, respectively. Scavenger studies showed that $^{\cdot}O_2^-$ played an important role, while, h$^+$ and HO$^{\cdot}$ also played significant roles in the photodegradation of MB dye. The CSNG-2 nanocomposite showed good recyclability and photostability in five consecutive cycles with a loss of just ~1%. Thus, the synergistic effect and interface of the NG and CS heterostructures displayed a significant response in visible light absorption and also decreased the rate of recombination of photo-excited carriers, which enhanced the overall rate of reaction. Therefore, our study shows that the CSNG nanocomposite provides new insights into the adsorption ability and photocatalytic degradation of organic pollutants.

Author contributions

Sai Bhargava Vuggili: methodology, conceptualization, validation, formal analysis, investigation, resources, writing – original draft, visualization. Umesh Kumar: resources. Manu Sharma: conceptualization, methodology, writing – manuscript & editing, supervision, project administration.

Conflicts of interest

The authors declare no conflict of interest.

Acknowledgements

References

1 D. Chen, Y. Cheng, N. Zhou, P. Chen, Y. Wang, K. Li, S. Huo, P. Cheng, P. Peng, R. Zhang and L. Wang, Photocatalytic degradation of organic pollutants using TiO$_2$-based photocatalysts: A review, *J. Cleaner Prod.*, 2020 Sep 20, **268**, 121725, DOI: **10.1016/j.jclepro.2020.121725**.

2 S. Li, M. Cai, Y. Liu, J. Zhang, C. Wang, S. Zang, Y. Li, P. Zhang and X. Li, In situ construction of a C$_3$N$_5$ nanosheet/Bi$_2$WO$_6$ nanodot S-scheme heterojunction with enhanced structural defects for the efficient photocatalytic removal of tetracycline and Cr (vi), *Inorg. Chem. Front.*, 2022, **9**(11), 2479–2497, DOI: **10.1039/D2QI00317A**.

3 C. C. Wang, J. R. Li, X. L. Lv, Y. Q. Zhang and G. Guo, Photocatalytic organic pollutants degradation in metal–organic frameworks, *Energy Environ. Sci.*, 2014, 7(9), 2831–2867, DOI: **10.1039/C4EE01299B**.

4 Q. Liu, X. Zhu, L. Zhong, S. Zhang, X. Luo, Q. Liu, L. Tang and Y. Lu, Recent advances in the applications of nanozymes for the efficient detection/removal of organic pollutants: a review, *Environ. Sci.: Nano*, 2022, **9**, 1212–1235, DOI: **10.1039/D2EN00027J**.

5 N. Modirshahla, M. A. Behnajady, R. Rahbarfam and A. Hassani, Effects of operational parameters on decolorization of CI Acid Red 88 by UV/H$_2$O$_2$ process: evaluation of electrical energy consumption, *Clean: Soil, Air, Water*, 2012, **40**(3), 298–302, DOI: **10.1002/clen.201000574**.

6 A. K. Mohammed and D. Shetty, Macroscopic covalent organic framework architectures for water remediation, *Environ. Sci.: Water Res. Technol.*, 2021, 7(11), 1895–1927, DOI: **10.1039/D1EW00408E**.

7 K. S. Varma, R. J. Tayade, K. J. Shah, P. A. Joshi, A. D. Shukla and V. G. Gandhi, Photocatalytic degradation of pharmaceutical and pesticide compounds (PPCs) using doped TiO$_2$ nanomaterials: A review, *Water-Energy Nexus*, 2020, 3, 46–61, DOI: **10.1016/j.wen.2020.03.008**.

8 P. C. Nagajyothi, S. V. Prabhakar Vattikuti, K. C. Devarayapalli, K. Yoo, J. Shim and T. V. Sreekanth, Green synthesis: Photocatalytic degradation of textile dyes using metal and metal oxide nanoparticles-latest trends

and advancements, *Crit. Rev. Environ. Sci. Technol.*, 2020, **50**(24), 2617–2723, DOI: 10.1080/10643389.2019.1705103.

9 P. Maurya and R. Kumari, Toxic metals distribution, seasonal variations and environmental risk assessment in surficial sediment and mangrove plants (A. marina), Gulf of Kachchh (India), *J. Hazard. Mater.*, 2021, **413**, 125345, DOI: 10.1016/j.jhazmat.2021.125345.

10 S. Sarkar, N. T. Ponce, A. Banerjee, R. Bandopadhyay, S. Rajendran and E. Lichtfouse, Green polymeric nanomaterials for the photocatalytic degradation of dyes: a review, *Environ. Chem. Lett.*, 2020, **18**, 1569–1580, DOI: 10.1007/s10311-020-01021-w.

11 J. B. Grimm, A. N. Tkachuk, L. Xie, H. Choi, B. Mohar, N. Falco, K. Schaefer, R. Patel, Q. Zheng, Z. Liu and J. Lippincott-Schwartz, A general method to optimize and functionalize red-shifted rhodamine dyes, *Nat. Methods*, 2020, **17**(8), 815–821, DOI: 10.1038/s41592-020-0909-6.

12 A. Tkaczyk, K. Mitrowska and A. Posyniak, Synthetic organic dyes as contaminants of the aquatic environment and their implications for ecosystems: A review, *Sci. Total Environ.*, 2020, **717**, 137222, DOI: 10.1016/j.scitotenv.2020.137222.

13 K. Hu, P. Liu, Z. Zhang, J. Bian, G. Wang, H. Wu, H. Xu and L. Jing, Improved photocatalytic activities of g-C_3N_4 nanosheets by B doping and Ru-Oxo cluster modification for CO_2 conversion, *J. Phys. Chem. C*, 2022, **126**(23), 9704–9712, DOI: 10.1021/acs.jpcc.2c01919.

14 P. Maurya and R. Kumari, Spatiotemporal variation of the nutrients and heavy metals in mangroves using multivariate statistical analysis, Gulf of Kachchh (India), *Environ. Res.*, 2021, **195**, 110803, DOI: 10.1016/j.envres.2021.110803.

15 M. M. Khin, A. S. Nair, V. J. Babu, R. Murugan and S. Ramakrishna, A review on nanomaterials for environmental remediation, *Energy Environ. Sci.*, 2012, **5**(8), 8075–8109, DOI: 10.1039/C2EE21818F.

16 K. Kadiya, S. B. Vuggili, U. K. Gaur and M. Sharma, Comparative photocatalytic dye and drug degradation study using efficient visible light-induced silver phosphate nanoparticles, *Environ. Sci. Pollut. Res.*, 2021, **28**, 46390–46403, DOI: 10.1007/s11356-020-10982-y.

17 A. Hassani, S. Krishnan, J. Scaria, P. Eghbali and P. V. Nidheesh, Z-scheme photocatalysts for visible-light-driven pollutants degradation: a review on recent advancements, *Curr. Opin. Solid State Mater. Sci.*, 2021, **25**(5), 100941, DOI: 10.1016/j.cossms.2021.100941.

18 M. Sharma, D. Das, A. Baruah, A. Jain and A. K. Ganguli, Design of porous silica supported tantalum oxide hollow spheres showing enhanced photocatalytic activity, *Langmuir*, 2014, **30**(11), 3199–3208, DOI: 10.1021/la500167a.

19 R. Shen, L. Zhang, N. Li, Z. Lou, T. Ma, P. Zhang, Y. Li and X. Li, W–N bonds precisely boost Zscheme interfacial charge transfer in g-C3N4/WO3 heterojunctions for enhanced photocatalytic H2 evolution, *ACS Catal.*, 2022, **12**(16), 9994–10003, DOI: 10.1021/acscatal.2c02416.

20 L. Biswal, S. Nayak and K. Parida, Recent progress on strategies for the preparation of 2D/2D MXene/g-C_3N_4 nanocomposites for photocatalytic energy and environmental applications, *Catal. Sci. Technol.*, 2021, **11**(4), 1222–1248, DOI: 10.1039/D0CY02156C.

21 X. Liu, J. Iocozzia, Y. Wang, X. Cui, Y. Chen, S. Zhao, Z. Li and Z. Lin, Noble metal–metal oxide nanohybrids with tailored nanostructures for efficient solar energy conversion, photocatalysis and environmental remediation, *Energy Environ. Sci.*, 2017, **10**(2), 402–434, DOI: 10.1039/C6EE02265K.

22 Y. Li, M. Gu, X. Zhang, J. Fan, K. Lv, S. A. Carabineiro and F. Dong, 2D g-C_3N_4 for advancement of photo-generated carrier dynamics: status and challenges, *Mater. Today*, 2020, **41**, 270–303, DOI: 10.1016/j.mattod.2020.09.004.

23 S. Saha, K. Ojha, M. Sharma and A. K. Ganguli, Ni_3Co/G alloy as an earth-abundant robust and stable electrocatalyst for the hydrogen evolution reaction, *New J. Chem.*, 2017, **41**(13), 5916–5923, DOI: 10.1039/C7NJ00364A.

24 C. Yang, Q. Tan, Q. Li, J. Zhou, J. Fan, B. Li, J. Sun and K. Lv, 2D/2D Ti_3C_2 MXene/g-C_3N_4 nanosheets heterojunction for high efficient CO_2 reduction photocatalyst: Dual effects of urea, *Appl. Catal., B*, 2020, **268**, 118738, DOI: 10.1016/j.apcatb.2020.118738.

25 S. B. Vuggili, K. Kadiya, U. K. Gaur and M. Sharma, Synthesis of graphitic carbon nitride/cadmium sulfide core-shell nanofibers for enhanced photocatalysis, *Environ. Sci. Pollut. Res.*, 2021, **28**, 46377–46389, DOI: 10.1007/s11356-020-10568-8.

26 V. S. Bhargava, G. Singh and M. Sharma, Synergistic properties of graphitic carbon nitride/cerium molybdate nanocomposites for enhanced photocatalytic activity, in *AIP Conference Proceedings*, AIP Publishing LLC, 2018, vol. 1961, no. 1, p. 030006, DOI: 10.1063/1.5035208.

27 S. B. Vuggili, S. K. Khanth, K. Kadiya, U. K. Gaur and M. Sharma, Improvement in visible light stimulated photocatalysis by the inducement of magnesium dopant inside graphitic carbon nitride frameworks, *J. Environ. Chem. Eng.*, 2019, **7**(6), 103440, DOI: 10.1016/j.jece.2019.103440.

28 M. Sharma, S. Vaidya and A. K. Ganguli, Enhanced photocatalytic activity of g-C_3N_4-TiO_2 nanocomposites for degradation of Rhodamine B dye, *J. Photochem. Photobiol., A*, 2017, **335**, 287–293, DOI: 10.1016/j.jphotochem.2016.12.002.

29 S. B. Vuggili, U. K. Gaur and M. Sharma, 2D/2D facial interaction of nitrogen-doped g-C_3N_4/In_2S_3 nanosheets for high performance by visible-light-induced photocatalysis, *J. Alloys Compd.*, 2022, **902**, 163757, DOI: 10.1016/j.jallcom.2022.163757.

30 T. Zhang, G. V. Lowry, N. L. Capiro, J. Chen, W. Chen, Y. Chen, D. D. Dionysiou, D. W. Elliott, S. Ghoshal, T. Hofmann and H. Hsu-Kim, *In situ* remediation of subsurface contamination: opportunities and challenges for nanotechnology and advanced materials, *Environ. Sci.: Nano*, 2019, **6**(5), 1283–1302, DOI: 10.1039/C9EN00143C.

31 Q. Yu, Q. Xu, H. Li, K. Yang and X. Li, Effects of heat treatment on the structure and photocatalytic activity of polymer carbon nitride, *J. Mater. Sci.*, 2019, **54**(23), 14599–14608, DOI: 10.1007/s10853-019-03895-w.

32 X. Miao, X. Yue, Z. Ji, X. Shen, H. Zhou, M. Liu, K. Xu, J. Zhu, G. Zhu, L. Kong and S. A. Shah, Nitrogen-doped carbon dots decorated on g-C₃N₄/Ag₃PO₄ photocatalyst with improved visible light photocatalytic activity and mechanism insight, *Appl. Catal., B*, 2018, **227**, 459–469, DOI: **10.1016/j.apcatb.2018.01.057**.

33 G. Liao, Y. Gong, L. Zhang, H. Gao, G. J. Yang and B. Fang, Semiconductor polymeric graphitic carbon nitride photocatalysts: the "holy grail" for the photocatalytic hydrogen evolution reaction under visible light, *Energy Environ. Sci.*, 2019, **12**(7), 2080–2147, DOI: **10.1039/C9EE00717B**.

34 L. Lei, D. Huang, C. Zhang, R. Deng, S. Chen and Z. Li, F dopants triggered active sites in bifunctional cobalt sulfide@nickel foam toward electrocatalytic overall water splitting in neutral and alkaline media: Experiments and theoretical calculations, *J. Catal.*, 2020, **385**, 129–139, DOI: **10.1016/j.jcat.2020.03.012**.

35 R. Zahra, E. Pervaiz, M. Yang, O. Rabi, Z. Saleem, M. Ali and S. Farrukh, A review on nickel cobalt sulphide and their hybrids: Earth abundant, pH stable electro-catalyst for hydrogen evolution reaction, *Int. J. Hydrogen Energy*, 2020, **45**(46), 24518–24543, DOI: **10.1016/j.ijhydene.2020.06.236**.

36 W. Dou, W. Yang, X. Zhao and Q. Pan, Hollow cobalt sulfide for highly efficient uranium adsorption from aqueous solutions, *Inorg. Chem. Front.*, 2019, **6**(11), 3230–3236, DOI: **10.1039/C9QI00737G**.

37 A. A. Khan, S. Kumari, A. Chowdhury and S. Hussain, Phase tuned originated dual properties of cobalt sulfide nanostructures as photocatalyst and adsorbent for removal of dye pollutants, *ACS Appl. Nano Mater.*, 2018, **1**(7), 3474–3485, DOI: **10.1021/acsanm.8b00656**.

38 H. Liu, Z. You, S. Yang, C. Liu, X. Xie, K. Xiang, X. Wang and X. Yan, High-efficient adsorption and removal of elemental mercury from smelting flue gas by cobalt sulfide, *Environ. Sci. Pollut. Res.*, 2019, **26**, 6735–6744, DOI: **10.1007/s11356-019-04159-5**.

39 S. B. Khan, M. S. Khan, K. Akhtar, E. M. Bakhsh, T. Kamal, A. M. Asiri and Y. Shen, Design of efficient solar photocatalytic system for hydrogen production and degradation of environmental pollutant, *J. Mater. Res. Technol.*, 2021, **14**, 2497–2512, DOI: **10.1016/j.jmrt.2021.07.097**.

40 C. K. Maity, N. Goswami, K. Verma, S. Sahoo and G. C. Nayak, A facile synthesis of boron nitride supported zinc cobalt sulfide nano hybrid as high-performance pseudocapacitive electrode material for asymmetric supercapacitors, *J. Energy Storage*, 2020, **32**, 101993, DOI: **10.1016/j.est.2020.101993**.

41 W. Li, S. Li, Y. Tang, X. Yang, W. Zhang, X. Zhang, H. Chai and Y. Huang, Highly efficient activation of peroxymonosulfate by cobalt sulfide hollow nanospheres for fast ciprofloxacin degradation, *J. Hazard. Mater.*, 2020, **389**, 121856, DOI: **10.1016/j.jhazmat.2019.121856**.

42 L. Amirache, F. Barka-Bouaifel, P. Borthakur, M. R. Das, H. Ahouari, H. Vezin, A. Barras, B. Ouddane, S. Szunerits and R. Boukherroub, Cobalt sulfide-reduced graphene

oxide: An efficient catalyst for the degradation of rhodamine B and pentachlorophenol using peroxymonosulfate, *J. Environ. Chem. Eng.*, 2021, **9**(5), 106018, DOI: **10.1016/j.jece.2021.106018**.

43 P. I. Hora, P. J. Novak and W. A. Arnold, Photodegradation of pharmaceutical compounds in partially nitritated wastewater during UV irradiation, *Environ. Sci.: Water Res. Technol.*, 2019, **5**(5), 897–909, DOI: **10.1039/C8EW00714D**.

44 Y. Bian, Y. Ma, Y. Shang, P. Tan and J. Pan, Self-integrated β-Bi₂O₃/Bi₂O₂@Bi₂O₂CO₃ ternary composites: formation mechanism and visible light photocatalytic activity, *Appl. Surf. Sci.*, 2018, **430**, 613–624, DOI: **10.1016/j.apsusc.2017.06.063**.

45 A. Deng, C. Yu, Z. Xue, J. Huang, H. Pan and L. Pei, Rare metal doping of the hexahydroxy strontium stannate with enhanced photocatalytic performance for organic pollutants, *J. Mater. Res. Technol.*, 2022, **19**, 1073–1089, DOI: **10.1016/j.jmrt.2022.05.104**.

46 S. Khanchandani, S. Kumar and A. K. Ganguli, Comparative study of TiO₂/CuS core/shell and composite nanostructures for efficient visible light photocatalysis, *ACS Sustainable Chem. Eng.*, 2016, **4**(3), 1487–1499, DOI: **10.1021/acssuschemeng.5b01460**.

47 P. Praus, On electronegativity of graphitic carbon nitride, *Carbon*, 2021, **172**, 729–732, DOI: **10.1016/j.carbon.2020.10.074**.

48 Z. Z. Vasiljevic, M. P. Dojcinovic, J. D. Vujancevic, I. Jankovic-Castvan, M. Ognjanovic, N. B. Tadic, S. Stojadinovic, G. O. Brankovic and M. V. Nikolic, Photocatalytic degradation of methylene blue under natural sunlight using iron titanate nanoparticles prepared by a modified sol–gel method, *R. Soc. Open Sci.*, 2020, **7**(9), 200708, DOI: **10.1098/rsos.200708**.

49 Z. Liu, J. Xu, Q. Liang, Y. Li and H. Yu, CoS/ZnWO₄ composite with band gap matching: simple impregnation synthesis, efficient dye sensitization system for hydrogen production, *J. Nanopart. Res.*, 2020, **22**, 1, DOI: **10.1007/s11051-020-04857-z**.

50 S. Peng, X. Han, L. Li, Z. Zhu, F. Cheng, M. Srinivansan, S. Adams and S. Ramakrishna, Unique cobalt sulfide/reduced graphene oxide composite as an anode for sodium-ion batteries with superior rate capability and long cycling stability, *Small*, 2016, **12**(10), 1359–1368, DOI: **10.1002/smll.201502788**.

51 A. C. Ferrari and J. Robertson, Interpretation of Raman spectra of disordered and amorphous carbon, *Phys. Rev. B: Condens. Matter Mater. Phys.*, 2000, **61**(20), 14095, DOI: **10.1103/PhysRevB.61.14095**.

52 J. Li, Y. Zhang, X. Zhang, J. Han, Y. Wang, L. Gu, Z. Zhang, X. Wang, J. Jian, P. Xu and B. Song, Direct transformation from graphitic C₃N₄ to nitrogen-doped graphene: an efficient metal-free electrocatalyst for oxygen reduction reaction, *ACS Appl. Mater. Interfaces*, 2015, **7**(35), 19626–19634, DOI: **10.1021/acsami.5b03845**.

53 D. Ma, B. Hu, W. Wu, X. Liu, J. Zai, C. Shu, T. Tadesse Tsega, L. Chen, X. Qian and T. L. Liu, Highly active nanostructured CoS₂/CoS heterojunction electrocatalysts for aqueous

polysulfide/iodide redox flow batteries, *Nat. Commun.*, 2019, **10**(1), 3367, DOI: 10.1038/s41467-019-11176-y.

54 S. Dong, Z. Zeng, W. Cai, Z. Zhou, C. Dou, H. Liu and J. Xia, The zeta potentials of g-C$_3$N$_4$ nanoparticles: Effect of electrolyte, ionic strength, pH, and humic acid, *J. Nanopart. Res.*, 2019, **21**, 1–2, DOI: 10.1007/s11051-019-4686-z.

55 H. Sheng, A. N. Janes, R. D. Ross, D. Kaiman, J. Huang, B. Song, J. R. Schmidt and S. Jin, Stable and selective electrosynthesis of hydrogen peroxide and the electro-Fenton process on CoSe$_2$ polymorph catalysts, *Energy Environ. Sci.*, 2020, **13**(11), 4189–4203.

56 Q. Shao, X. Liu, J. Dong, L. Liang, Q. zhang, P. Li, S. Yang, X. Zang and N. Cao, Vulcanization Conditions of Bimetallic Sulfides Under Different Sulfur Sources for Supercapacitors: A Review, *J. Electron. Mater.*, 2023, 1–6, DOI: 10.1007/s11664-022-10167-y.

57 V. K. Gupta, I. Tyagi, S. Agarwal, R. Singh, M. Chaudhary, A. Harit and S. Kushwaha, Column operation studies for the removal of dyes and phenols using a low cost adsorbent, *Global J. Environ. Sci. Manage.*, 2016, **2**(1), 1, DOI: 10.7508/GJESM.2016.01.001.

58 J. Li, X. Xiao, X. Xu, J. Lin, Y. Huang, Y. Xue, P. Jin, J. Zou and C. Tang, Activated boron nitride as an effective adsorbent for metal ions and organic pollutants, *Sci. Rep.*, 2013, **3**(1), 1–7, DOI: 10.1038/srep03208.

59 B. Zhu, Q. Xu, X. Bao, D. Lu, H. Yin, Y. Qin and X. C. Shen, g-C$_3$N$_4$/CoNiFe-LDH Z-scheme heterojunction for efficient CO$_2$ photoreduction and MB dye photodegradation, *Catal. Sci. Technol.*, 2021, **11**(23), 7727–7739, DOI: 10.1039/D1CY01475G.

60 P. Maurya, R. Kumari and S. Mukherjee, Hydrochemistry in integration with stable isotopes (δ^{18}O and δD) to assess seawater intrusion in coastal aquifers of Kachchh district, Gujarat, India, *J. Geochem. Explor.*, 2019, **196**, 42–56, DOI: 10.1016/j.gexplo.2018.09.013.

61 N. Tavker, U. K. Gaur and M. Sharma, Agro-waste extracted cellulose supported silver phosphate nanostructures as a green photocatalyst for improved photodegradation of RhB dye and industrial fertilizer effluents, *Nanoscale Adv.*, 2020, **2**(7), 2870–2884, DOI: 10.1039/D0NA00181C.

62 M. Spangenberg, J. I. Bryant, S. J. Gibson, P. J. Mousley, Y. Ramachers and G. R. Bell, Ultraviolet absorption of contaminants in water, *Sci. Rep.*, 2021, **11**(1), 1–8, DOI: 10.1038/s41598-021-83322-w.

63 S. Kumar, A. Kumar, A. Kumar, R. Balaji and V. Krishnan, Highly efficient visible light active 2D-2D nanocomposites of N-ZnO-g-C$_3$N$_4$ for photocatalytic degradation of diverse industrial pollutants, *ChemistrySelect*, 2018, **3**(6), 1919–1932, DOI: 10.1002/slct.201703156.

64 X. Bai, X. Wang, X. Lu, S. Hou, B. Sun, C. Wang, T. Jia and S. Yang, High crystallinity and conjugation promote the polarization degree in O-doped g-C$_3$N$_4$ for removing organic pollutants, *CrystEngComm*, 2021, **23**(6), 1366–1376, DOI: 10.1039/D0CE01776K.

65 A. Hassani, M. Faraji and P. Eghbali, Facile fabrication of mpg-C$_3$N$_4$/Ag/ZnO nanowires/Zn photocatalyst plates for photodegradation of dye pollutant, *J. Photochem. Photobiol., A*, 2020, **400**, 112665, DOI: 10.1016/j.jphotochem.2020.112665.

66 F. Ge, S. Huang, J. Yan, L. Jing, F. Chen, M. Xie, Y. Xu, H. Xu and H. Li, Sulfur promoted n-π* electron transitions in thiophene-doped g-C$_3$N$_4$ for enhanced photocatalytic activity, *Chin. J. Catal.*, 2021, **42**(3), 450–459, DOI: 10.1016/S1872-2067(20)63674-9.

67 Y. Huang, L. Ning, Z. Feng, G. Ma, S. Yang, Y. Su, Y. Hong, H. Wang, L. Peng and J. Li, Graphitic carbon nitride nanosheets with low O N$_1$-doping content as efficient photocatalysts for organic pollutant degradation, *Environ. Sci.: Nano*, 2021, **8**(2), 460–469, DOI: 10.1039/D0EN01198.

68 W. Zhang, Y. Ma, X. Zhu, S. Liu, T. An, J. Bao, X. Hu and H. Tian, Fabrication of Ag decorated g-C$_3$N$_4$/LaFeO$_3$ Z-scheme heterojunction as highly efficient visible-light photocatalyst for degradation of methylene blue and tetracycline hydrochloride, *J. Alloys Compd.*, 2021, **864**, 158914, DOI: 10.1016/j.jallcom.2021.158914.

69 P. J. Mafa, M. E. Malefane, A. O. Idris, D. Liu, J. Gui, B. B. Mamba and A. T. Kuvarega, Multi-elemental doped g-C$_3$N$_4$ with enhanced visible light photocatalytic activity: insight into naproxen degradation, kinetics, effect of electrolytes, and mechanism, *Sep. Purif. Technol.*, 2022, **282**, 120089, DOI: 10.1016/j.seppur.2021.120089.

70 M. Jourshabani, Z. Shariatinia and A. Badiei, Synthesis and characterization of novel Sm$_2$O$_3$/S-doped g-C$_3$N$_4$ nanocomposites with enhanced photocatalytic activities under visible light irradiation, *Appl. Surf. Sci.*, 2018, **427**, 375–387, DOI: 10.1016/j.apsusc.2017.08.051.

71 D. Wang, X. Dong, Y. Lei, C. Lin, D. Huang, X. Yu and X. Zhang, Fabrication of Mn/P co-doped hollow tubular carbon nitride by a one-step hydrothermal–calcination method for the photocatalytic degradation of organic pollutants, *Catal. Sci. Technol.*, 2022, **12**(18), 5709–5722, DOI: 10.1039/D2CY01107G.

72 H. Chen, X. Zhang, L. Jiang, X. Yuan, J. Liang, J. Zhang, H. Yu, W. Chu, Z. Wu, H. Li and Y. Li, Strategic combination of nitrogen-doped carbon quantum dots and g-C$_3$N$_4$: efficient photocatalytic peroxydisulfate for the degradation of tetracycline hydrochloride and mechanism insight, *Sep. Purif. Technol.*, 2021, **272**, 118947, DOI: 10.1016/j.seppur.2021.118947.

73 G. Wang, Y. Zhao, H. Ma, C. Zhang, X. Dong and X. Zhang, Enhanced peroxymonosulfate activation on dual active sites of N vacancy modified g-C$_3$N$_4$ under visible-light assistance and its selective removal of organic pollutants, *Sci. Total Environ.*, 2021, **756**, 144139, DOI: 10.1016/j.scitotenv.2020.144139.

74 J. Jiang, X. Wang, C. Yue, S. Liu, Y. Lin, T. Xie and S. Dong, Efficient photoactivation of peroxymonosulfate by Z-scheme nitrogen-defect-rich NiCo$_2$O$_4$/g-C$_3$N$_4$ for rapid emerging pollutants degradation, *J. Hazard. Mater.*, 2021, **414**, 125528, DOI: 10.1016/j.jhazmat.2021.125528.

75 H. Song, Z. Guan, D. Xia, H. Xu, F. Yang, D. Li and X. Li, Copper-oxygen synergistic electronic reconstruction on g-C$_3$N$_4$ for efficient non-radical catalysis for peroxydisulfate

© 2023 The Author(s). Published by the Royal Society of Chemistry

Environ. Sci.: Adv., 2023, **2**, 795–814 | 813

and peroxymonosulfate, *Sep. Purif. Technol.*, 2021, **257**, 117957, DOI: 10.1016/j.seppur.2020.117957.

76 A. R. Amani-Ghadim, A. Tarighati Sareshkeh, N. Nozad Ashan, H. Mohseni-Zonouz, S. M. Seyed Ahmadian, M. S. Seyed Dorraji, M. Gholinejad and F. Bayat, Photocatalytic activity enhancement of carbon-doped g-C_3N_4 by synthesis of nanocomposite with Ag_2O and α-Fe_2O_3, *J. Chin. Chem. Soc.*, 2021, **68**(11), 2118–2131, DOI: 10.1002/jccs.202100253.

77 E. Prabakaran, T. Velempini, M. Molefe and K. Pillay, Comparative study of KF, KCl and KBr doped with graphitic carbon nitride for superior photocatalytic degradation of methylene blue under visible light, *J. Mater. Res. Technol.*, 2021, **15**, 6340–6355, DOI: 10.1016/j.jmrt.2021.10.128.

78 C. Tian, X. Tao, S. Luo, Y. Qing, X. Lu, J. She and Y. Wu, Cellulose nanofibrils anchored Ag on graphitic carbon nitride for efficient photocatalysis under visible light, *Environ. Sci.: Nano*, 2018, **5**(9), 2129–2143, DOI: 10.1039/C8EN00570B.

79 L. X. Su, Z. Y. Liu, Y. L. Ye, C. L. Shen, Q. Lou and C. X. Shan, Heterostructured boron doped nanodiamonds@ g-C_3N_4 nanocomposites with enhanced photocatalytic capability under visible light irradiation, *Int. J. Hydrogen Energy*, 2019, **44**(36), 19805–19815, DOI: 10.1016/j.ijhydene.2019.05.135.

80 L. Guo-Min, W. Bing and W. Rui, g-C_3N_4/Ag/GO composite photocatalyst with efficient photocatalytic performance: synthesis, characterization, kinetic studies, toxicity assessment and degradation mechanism, *Chin. J. Struct. Chem.*, 2020, **39**(9), 1675–1688.